

Characterized Source Model for Simulating Strong Ground Motions during the 2008 Wenchuan Earthquake

by Susumu Kurahashi and Kojiro Irikura

Abstract Extremely valuable strong-motion records during the 2008 Wenchuan earthquake were obtained at a number of stations close to the source region. We estimate the characterized source model for simulating ground motions using the empirical Green's function (EGF) method and the hybrid method using strong-motion data from the earthquake. The characterized source model consists of several asperities with large slip in the entire rupture area of the earthquake. The locations of the asperities that generate strong motions were determined from the timing of pulse arrivals in observed records near the source fault. Because aftershock records of the earthquake had not been released yet, observed records from an aftershock (M_w 4.9) of the 2008 Iwate–Miyagi Nairiku earthquake (M_w 6.9), which occurred in the shallow inland crust of the northeastern region in Japan, are used as substitutes for the EGFs. The synthetic motions obtained by the EGF method agree well with the observed records with respect to acceleration and velocity waveforms in the period range of less than 2 s. Broader-band strong motions are simulated by the hybrid method, which combines the numerical method for periods longer than 2 s with the EGF method for periods shorter than 2 s. The best-fit source model was obtained with stress drop on each asperity of approximately 13 MPa. The ground motions numerically simulated at the Bajiao station (SFB) near an asperity and in the forward rupture direction show directivity effects that are too strong in comparison with the observed motions. We examined the influence of rupture-velocity fluctuation on the synthetic waveforms in the forward rupture direction near the asperity, finding that the forward directivity effects decrease with increase in velocity variances.

Introduction

The Wenchuan earthquake, having a moment magnitude of 7.9 (United States Geological Survey, USGS; see [Data and Resources](#) section), struck the western part of Sichuan Province, China, on 14 May 2008, resulting in approximately 70,000 fatalities and causing enormous damage to infrastructures and buildings. The causes of serious damage to structures can be attributed to the characteristics of the strong ground motions and the vulnerability of structures.

The earthquake occurred along the Longmen Shan thrust belt at the eastern margin of the Tibetan Plateau. The rupture started from Wenchuan and propagated toward the northeast, rupturing a total length of approximately 300 km. During this earthquake, extremely valuable strong-motion records were obtained at a number of stations close to the source region by the National Strong Motion Observation Network System of China (NSMONS, [Li et al., 2008](#)).

Thus far, only a small number of strong-motion records have been obtained from great inland earthquakes. A limited quantity of data in disaster areas near the source region were obtained during the Chi-Chi earthquake (M_w 7.6) and the

2002 Denali earthquake (M_w 7.9). During the 2002 Denali earthquake, valuable records were obtained at more than 55 strong-motion stations, including those at a station located approximately 3 km north of the surface rupture, where the observed maximum horizontal peak ground acceleration was approximately $0.35g$ (Asano *et al.*, 2005).

The strong-motion records will be very useful, not only in source modeling for estimating strong ground motion but also in clarifying the relationship between structural damage and strong ground motions through the reproduction of ground motions at damage sites. The slip distribution on the source fault of this earthquake has been estimated by the waveform inversion using the strong-motion data as well as the teleseismic and synthetic aperture radar (SAR) data. The distribution of collapse ratios of buildings determined by remote sensing ([Chendu Branch of the China Academy of Science, 2008](#)) is compared with the slip distribution determined by joint inversion of teleseismic data and the strong motion ([Koketsu et al., 2009](#)) in Figure 1. Places with high collapse ratios appear to be located near asperities with large

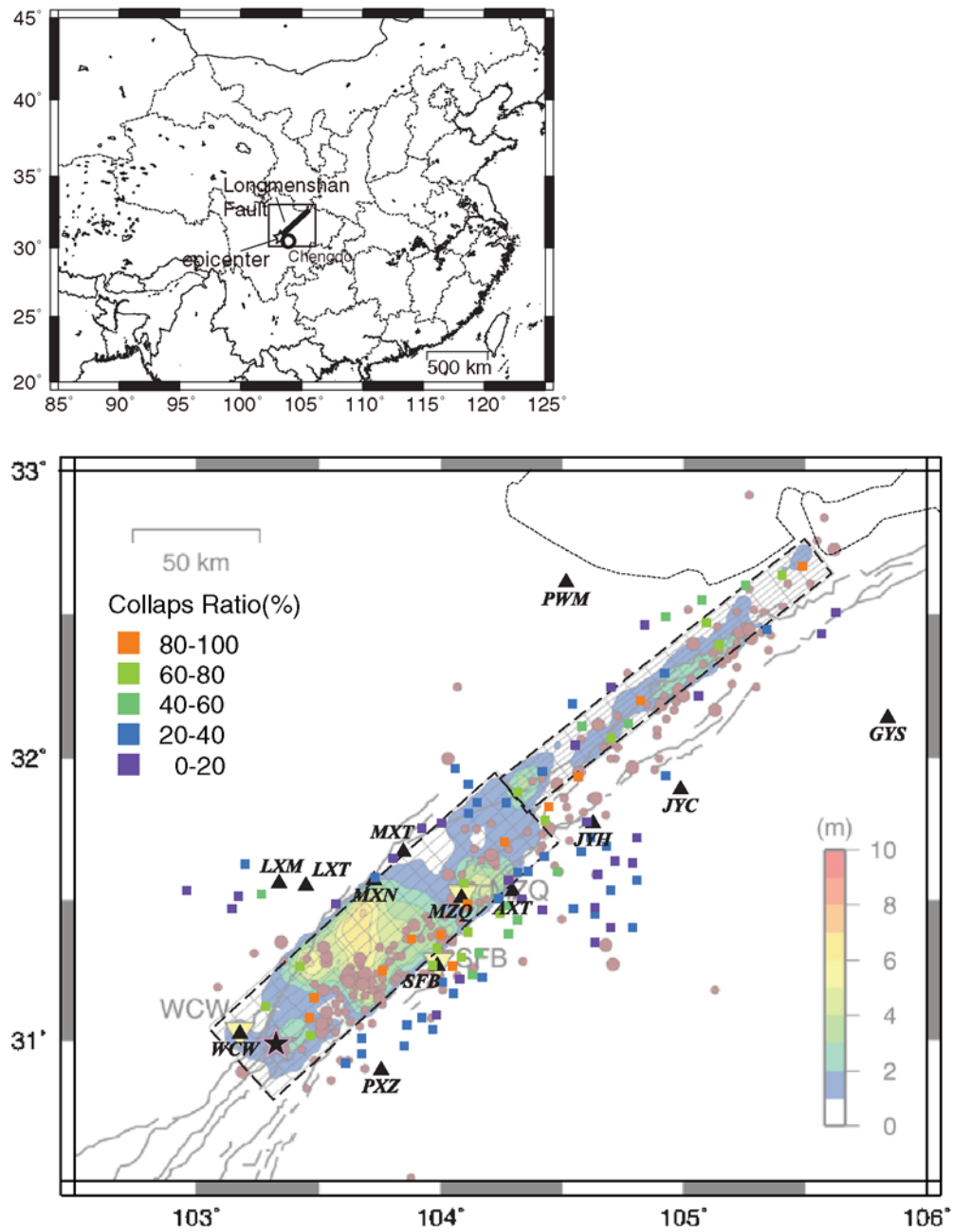


Figure 1. Distribution of slip on the fault plane and collapse ratios (squares) during the 2008 Wenchuan earthquake. The projection of the slip distribution onto the ground surface is obtained by the joint inversion of teleseismic and strong ground motion data (Koketsu *et al.*, 2009). The collapse ratios were estimated through remote sensing by the [Chendu Branch of the China Academy of Science \(2008\)](#). The star and triangle symbols indicate the hypocenter of the mainshock and the observation stations near the source area, respectively.

slip. Therefore, predicting strong ground motion is a critical factor for mitigating disasters caused by future earthquakes.

A scheme has been proposed for predicting strong ground motions from future crustal earthquakes (Irikura and Miyake, 2001; Irikura and Miyake, 2010). In this scheme, the source model is characterized by scaling relations for outer and inner fault parameters, based on studies of source processes inverted from strong-motion data and field investigations of active faults with high earthquake

potential. The outer fault parameters are the total seismic moment, the entire rupture area, and the average stress drop over the entire rupture area, and the inner fault parameters are the areas of asperities and the stress drop on each asperity inside the rupture area. This scheme is called the “recipe” for the prediction of strong ground motion by Irikura and Miyake (2001).

In the present study, we constructed the characterized source model for the Wenchuan earthquake and compared

the observed ground motions near the source fault with the synthetic ground motions using the empirical Green's function (EGF) method and the hybrid model. The characterized source model has several asperities with large slip in the entire rupture area of the earthquake. We then examine whether such fault parameters follow the scaling relationships used in the recipe. Finally, we discuss whether the recipe is applicable to the prediction of strong ground motions for magnitude-8 mega earthquakes occurring in inland crust.

Strong-Motion Data

Strong-motion records from the 2008 Wenchuan earthquake were obtained at 460 stations of the NSMONS. There are 12 stations within 20 km and 11 stations within 20–50 km of the source fault. The closest fault distance is 0.74 km at Qingping Station (MZQ), with a peak ground acceleration (PGA) of 824.1g; and the closest epicenter distance is 22.2 km at Wolong Station (WCW), with a PGA of 957.7g and a fault distance of 1.09 km ([China Earthquake Administration, 2008](#); [Li et al., 2008](#)).

In the present study, we used the observed records at eight stations near the source fault. The locations of the strong-motion stations are listed in Table 1. The strong-motion records at each station were obtained by three components of accelerometers on Earth surface, sampled at 200 or 500 Hz. The observed records were resampled at 100 Hz for the analysis. The resampled waveforms of acceleration were confirmed to be almost unchanged with respect to the amplitude and phase characteristics ranging up to the Nyquist frequency (50 Hz) and with respect to the maximum amplitude of each waveform, as compared to the originally observed waveforms.

Source Processes Inverted by Teleseismic, Strong-Motion, and SAR Data

Several authors have published the slip distributions from the waveform inversion of teleseismic and strong-motion data and from the inversion of Global Positioning System and SAR data ([Ji and Hayes, 2008](#); [Shen et al., 2008](#); [Wang et al., 2008](#); [Yarai et al., 2008](#); [Koketsu et al., 2009](#)). The source models used for the inversion have fault lengths ranging from 250 to 300 km, with strikes of approximately 230° and dips of approximately 35°. The segmentation of the source fault differs

Table 1
List of Locations of Strong-Motion Stations
Used in the Present Study

Station	Latitude (deg)	Longitude (deg)
AXT	104.3	31.54
JYH	104.63	31.78
MXN	103.73	31.58
MZQ	104.09	31.52
PXZ	103.76	30.91
SFB	103.99	31.28
WCW	103.18	31.04

depending on the study. For example, [Ji and Hayes \(2008\)](#) defined a one-segment source fault in the waveform inversion, whereas [Wang et al. \(2008\)](#) and [Koketsu et al. \(2009\)](#) defined a two-segment source fault.

The slip distributions inverted by the teleseismic data are shown in Figure 2a. The results obtained by the teleseismic data have common features. First, the rupture started near the southwest end of the source fault and propagated primarily unilaterally toward the northeast, with a main rupture length of approximately 250 km. Second, there are at least two significant asperities with large slip. Third, the largest asperity is located approximately 50 km northeast of the hypocenter, and a minor asperity is near the hypocenter.

A joint inversion combining the teleseismic data with the strong-motion records at six stations close to the source fault was performed by [Koketsu et al. \(2009\)](#). As shown in Figure 2b, the slip distribution obtained by the joint inversion suggests a more detailed rupture process with several asperities.

The inversion obtained by the SAR data was performed by [Yarai et al. \(2008\)](#), assuming a three-segment fault model. The strike and dip angles are different for each segment defined in Figure 2c. The locations of large slip areas appear to be similar to the results obtained by the joint inversion, although the segmentations are somewhat different.

Therefore, we adopt the slip distribution obtained by the joint inversion reported by [Koketsu et al. \(2009\)](#) as a reference source model because the asperities generating strong ground motions are imaged in detail.

Locations of Asperities Estimated From Strong-Motion Records

The strong-motion records near the source fault have some isolated pulses near the source fault, as shown on the acceleration and velocity waveforms in Figure 3 and Figure 4, respectively. Because these pulses were considered to be generated from the asperities, we attempted to locate the principal asperities on the rupture plane using arrival times of the prominent pulses on the records. The waveforms at six stations (WCW, SFB, MZQ, AXT, JYH, and JYC) located in the southwest-to-northeast direction along the Longmen Shan thrust belt in Figure 1 show the patterns of wave propagation from the asperities in Figure 3a and b. The travel times of the *S* waves generated from each asperity are shown by dotted lines in the figure.

The absolute trigger times of the records were not included in the dataset opened by the [China Earthquake Administration](#). Therefore, we first assumed that the average *P*-wave velocity (V_P) from the hypocenter to stations is 6 km/s, a velocity used in some references (e.g., [Liu et al., 2009](#)). The onsets of the *P* and *S* waves at these stations were determined by the Akaike information criteria (AIC; [Akaike, 1973](#); [Kitagawa, 1993](#)) as shown in Figure 4d and f. Then, the average *S*-wave velocity (V_S) from the hypocenter to stations was estimated to be 3.1 km/s from the time

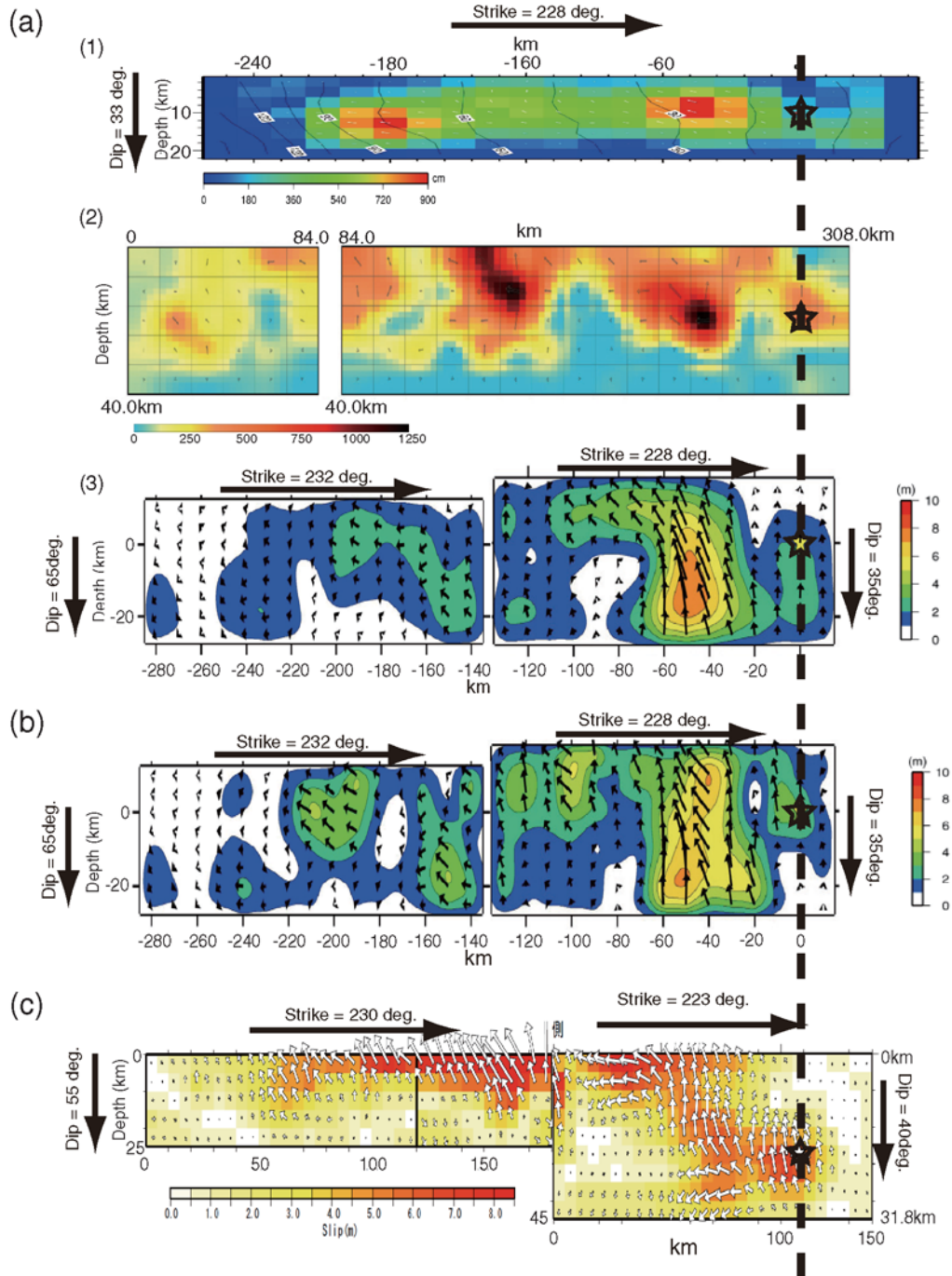


Figure 2. Slip distributions on the source fault during the 2008 Wenchuan earthquake. (a) Results obtained by the waveform inversion using the teleseismic data: (1) [Ji and Hayes \(2008\)](#), (2) [Wang et al. \(2008\)](#), and (3) [Koketsu et al. \(2009\)](#). (b) Results obtained by the joint inversion of the teleseismic and strong ground motion data ([Koketsu et al., 2009](#)). (c) Results obtained by the inversion of the interferometric synthetic aperture radar (InSAR) by the [Geographical Survey Institute \(2008\)](#). Stars indicate the hypocenter of the mainshock.

differences between the S -wave arrivals and the P -wave arrivals and the hypocentral distances at the stations.

In both Figure 3a and Figure 3b, the left-most dotted line shows the arrival of the S wave at station k (T_{1k}) from asperity 1, which is a small asperity near the hypocenter:

$$T_{1k} = R_{1k}/V_S \quad (1)$$

where R_{1k} is the propagation distance from asperity 1 to station k , and V_S is the velocity of the S wave. The lines labeled T_{2k} show the arrival of the S wave at station k from asperity 2, which is the largest asperity, located approximately 50 km from the hypocenter. Lines T_{3k} and T_{4k} correspond to the arrival times of the S waves at station k from asperity 3 and asperity 4, respectively.

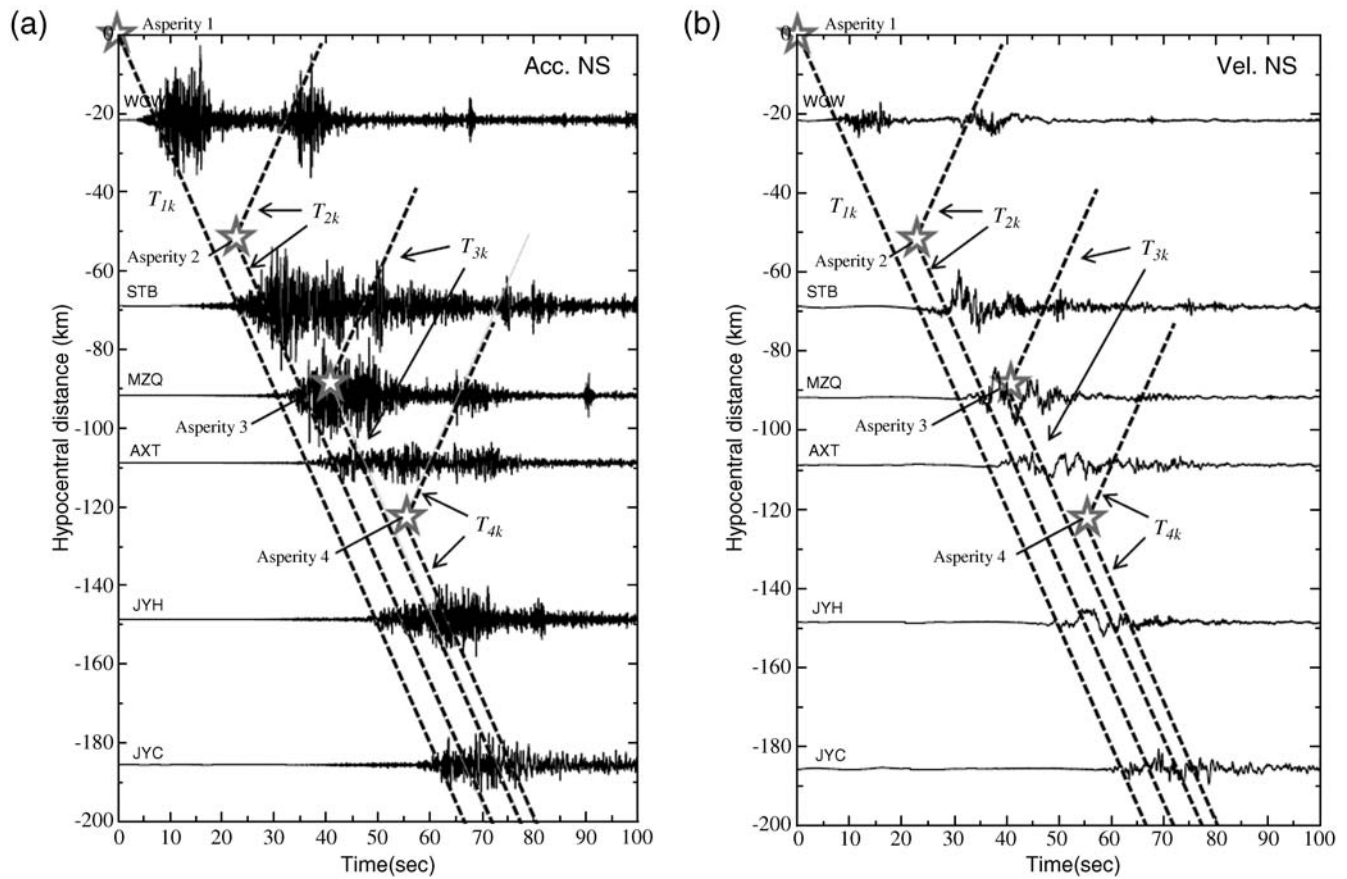


Figure 3. Observed records at six stations (WCW, SFB, MZQ, AXT, JYH, and JYC) for (a) acceleration and (b) velocity in the north-south (NS) component located along the source fault. The dotted lines indicate the travel times of the S waves generated from each asperity (T_{1k} , T_{2k} , T_{3k} , and T_{4k}). The open star symbols indicate the rupture start point of each asperity.

The onsets of the asperity pulses were determined by the minimum AIC procedure on the records at the stations where the pulses were detectable as distinctive pulses. The AIC value for the observed record at MZQ is calculated to detect the pulse generated from asperity 2, as shown in Figure 4h. We also estimated relative time differences between the corresponding pulses at different stations using cross correlation between two stations.

The locations of the asperities are determined using the following procedure. In the present study, the source model, including the rupture plane and the hypocenter (i.e., the rupture starting point on the rupture plane) is defined based on the inversion results obtained using the joint inversion by Koketsu *et al.* (2009). The hypocenter is estimated by the USGS. The southern and northern segments of the rupture plane are set to have similar strikes but different dip angles, based on the results of point source analyses; that is, a low dip angle of 35° for the southern segment and a high dip angle of 65° for the northern segment, as shown in Figure 1.

Next, we attempt to determine the locations of the asperities. The time difference between the S -wave arrival time from asperity j , T_{jk} , and that from the hypocenter, T_{0k} , at station k is given as

$$T_{jk} - T_{0k} = r_{0k}/V_r + R_{jk}/V_s - R_{0k}/V_s, \quad (2)$$

where r_{0j} is the rupture distance from the hypocenter to asperity j , R_{0k} is the propagation distance from the hypocenter to station k , R_{jk} is the propagation distance from asperity j to station k , and V_r is the rupture velocity.

In equation (2), $T_{jk} - T_{0k}$ is obtained from the observed record at each station, and R_{0k} is a known value obtained from the coordinates of the hypocenter and each station. As long as the records at more than four stations are used, then the locations of the asperities and V_r can be estimated in order to minimize the least mean square error.

Asperity 1 was assumed to be located at the hypocenter. The rupture velocity and the location of asperity 2 were estimated from the onsets of the pulselike waves at five stations (WCW, SFB, MZQ, AXT, and LXT). The optimum rupture velocity was estimated to be 2.9 km/s, which is close to the average rupture velocity adopted in the waveform inversion analysis by Koketsu *et al.* (2009). The standard error of the estimated location of asperity 2 is very small, as shown by a circle with a radius of about 3 km in Figure 5a. The clearly determined pulses from asperity 3 were detected only at two stations (MZQ and AXT). Then, the location of asperity 3 was estimated from the onsets at two stations,

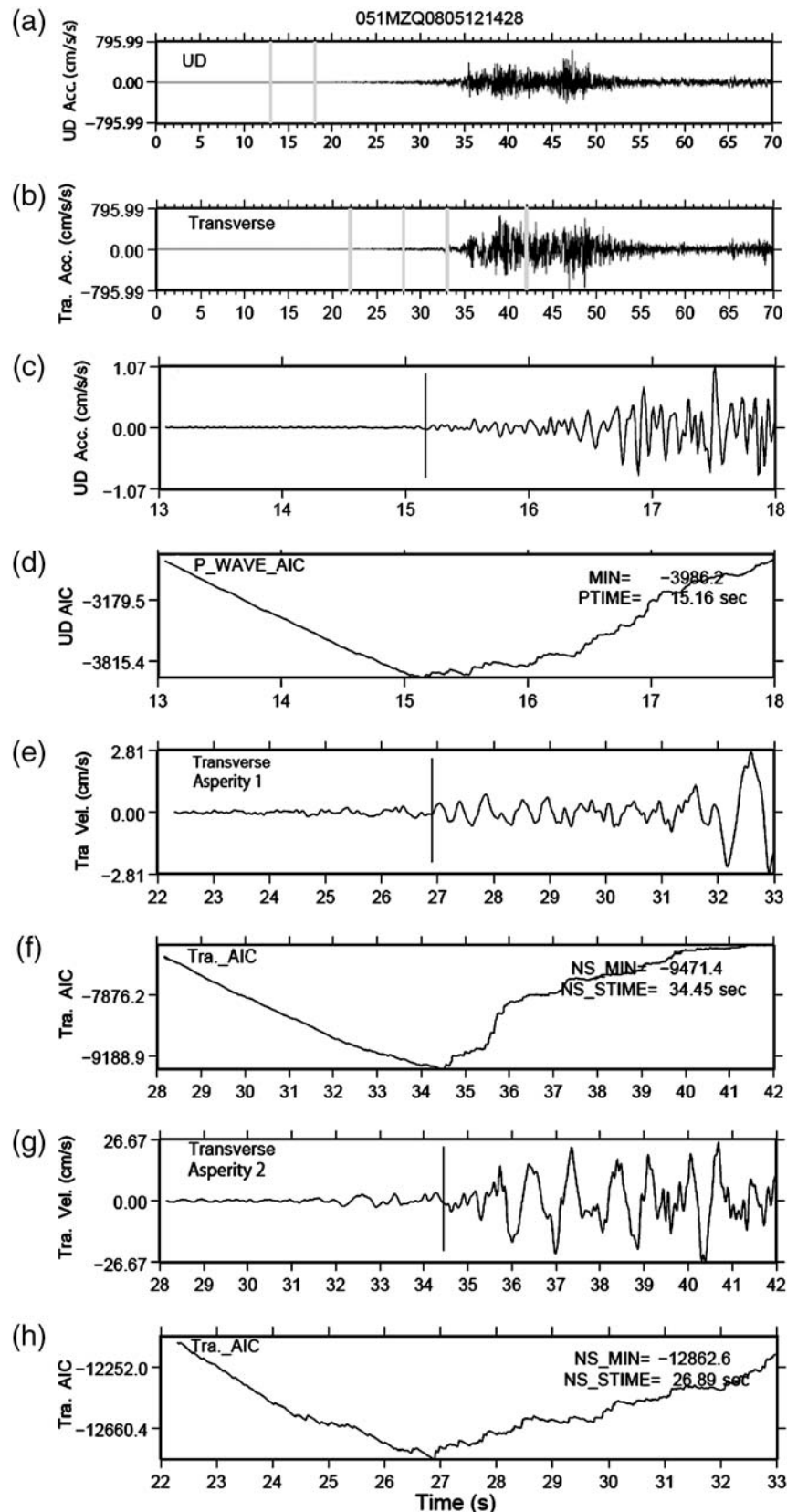


Figure 4. Extraction of onset times of *P* waves, *S* waves, and asperity pulses by the minimum Akaike information criteria (AIC) procedure at MZQ. (a) and (b) Waveforms of vertical and transverse components, respectively. (c) and (d) A closed-up waveform and AIC values of the vertical component around *P* wave onset. (e) and (f) A closed-up waveform and AIC values of the horizontal NS component around *S* wave onset. (g) and (h) Closed-up waveform and AIC values of the transverse component around the asperity pulse related to asperity 2.

assuming the rupture velocity of 2.9 km/s as shown in Figure 5b.

We found that asperity 4 was located in the northeastern segment after the rupture velocity was estimated to 2.9 km/s. In this paper, we limited estimation of ground motions from the southwestern segment. Therefore, we neglected asperity 4 in simulating ground motions.

Characterized Source Model and Ground-Motion Simulation in the Near-Source Area

Great inland earthquakes, such as the Wenchuan earthquake, produce catastrophic damage to buildings and facilities when they occur near cities. The causes of serious damage to buildings should be attributed to the characteristics

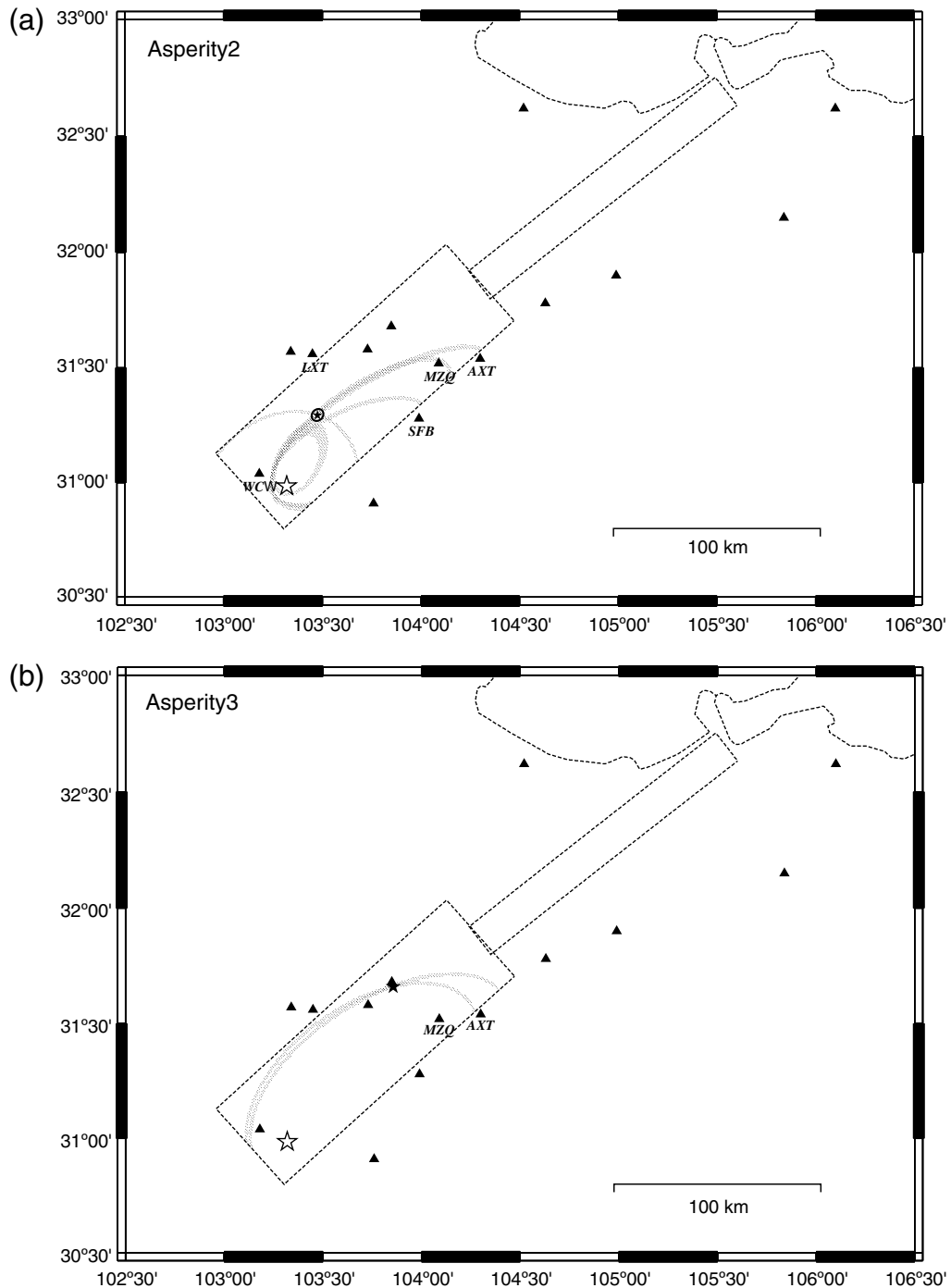


Figure 5. Estimation of locations of asperities. The rectangles indicate the two segments of the source fault obtained by Koketsu *et al.* (2009). The backpropagation lines (broken lines) from the observation stations (triangle) intersect each other around the locations of the asperities, as shown by star symbols. (a) Location of Asperity 2. (b) Location of Asperity 3.

of the strong ground motions and the vulnerability of buildings. In order to reduce the catastrophic effects of earthquakes, it is necessary to predict strong ground motions and improve the aseismic capacity of important buildings and critical facilities.

The strong ground motions are related to asperities with large slips rather than to the entire rupture area and total seismic moment. Based on the source characterization by Somerville *et al.* (1999), a characterized source model consisting of several asperities with large slip and a background region with less slip has been proposed (Irikura *et al.*, 2002; Miyake *et al.*, 2003).

An example of the characterized source model for the 1995 Kobe earthquake, which occurred along the Nojima–Rokko fault zone, Japan, is shown in Figure 6 (Kamae and Irikura, 1998). The slip distribution during the earthquake was inverted from the strong-motion data. The earthquake was characterized by a source model consisting of three asperities with large slip. The rupture velocity over the asperities and background area was taken to be constant. The area and stress drop of each asperity was estimated by comparing the simulated waveforms with observed waveforms. In the present study, we attempt to construct a characterized source model for simulating the ground motions from the Wenchuan earthquake. Broadband ground-motion simulations for great earthquakes with fault lengths exceeding 250 km and moment magnitudes of 8 have not yet been performed. In the present study, we use two methods for simulating strong ground motions, the empirical Green's function method (Irikura, 1986) and the hybrid method (e.g., Kamae *et al.*, 1998).

Ground Motion Simulation by the Empirical Green's Function (EGF) Method

The EGF method has been developed for the simulation of ground motions from the source fault of a large event using observed records of small events. The source fault is divided into $N \times N$ subfaults, the areas of which are taken to be equal to the fault area of the small event. The ground motions from the large event are expressed as a superposition of the records of small events as follows:

$$U(t) = C \sum_{i=1}^N \sum_{j=1}^N \frac{r}{r_{ij}} F(t - t_{ij}) * u(t), \quad (3)$$

where

$$t_{ij} = \frac{r_{ij} - r_0}{\beta} + \frac{\xi_{ij}}{V_R}, \quad (4)$$

$$F(t) = \delta(t) + \frac{1}{n'} \sum_{k=1}^{(N-1)n'} \delta \left[t - (k-1) \frac{\pi}{(N-1)n'} \right], \quad (5)$$

and $U(t)$ and $u(t)$ are the ground motion for the large event and the observed record of the small event used as the EGF, respectively. The terms r , r_{ij} , and r_0 are the respective dis-

tances from the site to the hypocenter of the small event, from the site to the (i, j) subfault, and from the site to the starting point of the rupture on the fault plane of the large event. The term ξ_{ij} is the distance between the starting point and the (i, j) subfault, β is the shear wave velocity, V_R is the rupture velocity, τ is the rise time or slip duration of the large event, and n' is an arbitrary integer number to shift the artificial periodicity to a frequency higher than that of interest. This EGF method was described in detail by Kamae and Irikura (1998).

In order to apply the EGF method to simulating ground motions, observed records from small events occurring in the mainshock source area are necessary. Unfortunately, thus far, we have no aftershock records of the Wenchuan earthquake. We therefore select appropriate ground motion records from small events that occurred in other regions as substitutes for the EGFs.

The advantage of the EGF method is that motions of small events have almost the same propagation-path effects and local-site effects as the mainshock. Another advantage is to adjust the difference of the source spectral-characteristics between the small and large events, considering the ω^2 source model (Brune, 1970). As long as the observed records from the small event used as the EGFs have spectral contents following the ω^2 source model, the ground motions simulated for the large event also have those following the ω^2 source model. In our analysis, each asperity corresponds to the large event mentioned previously. Therefore, ground motions simulated using the EGF method have short-period contents of engineering interest. On the other hand, theoretical simulation is limited to periods of longer than 2 s because of the difficulty in obtaining velocity structures of sufficient precision to calculate short-period motions. Another difficulty of theoretical simulation is that synthetic ground motions in the conventional waveform inversion analysis of strong-motion data have spectral contents with more rapid decay at high frequencies compared with the observed ground motions.

As the EGFs, we select observed records from the events for which (1) the source mechanism associated with the source effect, (2) the hypocentral distance related to the propagation-path effects, and (3) the surface geology related to the site effects are similar to those of the target event.

Then, for the simulation of strong ground motions for the Wenchuan earthquake, we used the observed records from an aftershock (M_w 4.9) of the 2008 Iwate–Miyagi Nairiku earthquake (M_w 6.9), which occurred in the shallow inland crust of the northeastern region in Japan. The mainshock was estimated to be a reverse fault with a strike to the southwest and a dip to the northwest (e.g., Suzuki *et al.*, 2008). As shown in Figure 7, similar to the Wenchuan earthquake, there are basins and mountains on the east and west sides of the surface fault, respectively. The focal mechanism of the aftershock was determined by F-net of the National Research Institute for Earth Science and Disaster Prevention (NIED); its projection onto the lower hemisphere is shown at the bottom left of Figure 7.

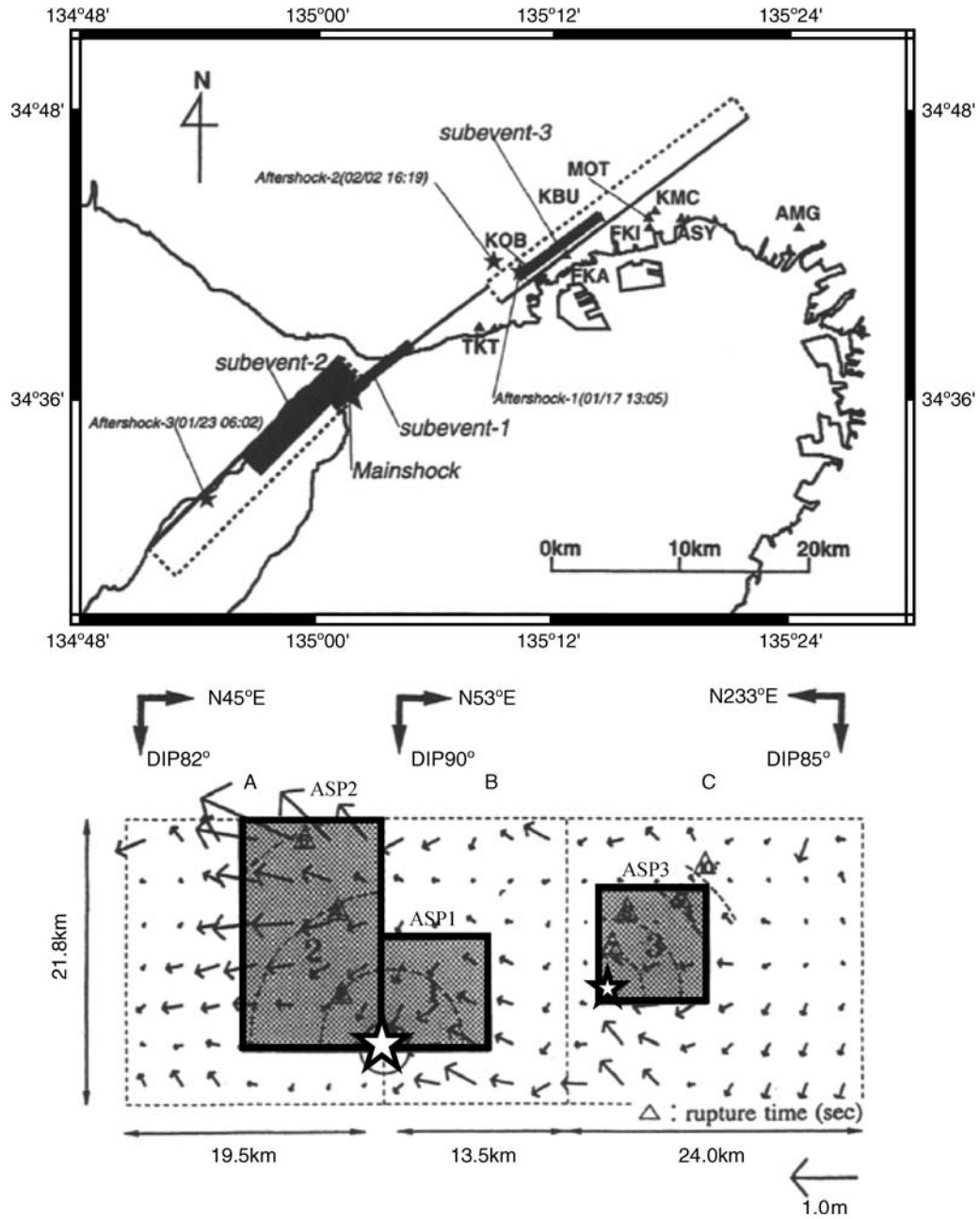


Figure 6. Example of the characterized source model. This model was constructed for simulating ground motions from the 1995 Kobe earthquake (Kamae and Irikura, 1998). The large star symbol indicates the hypocenter from which the rupture started, and the small star symbol indicates the rupture starting point of the small asperity.

Several strong-motion records from the aftershock were obtained at stations near the source fault in the basin area and in the mountainous region. These stations belong to the K-NET and KiK-net strong-motion observation networks, which are operated by NIED. For simulating ground motions at stations in the basin and mountain areas during the Wenchuan earthquake, the observed records of the aftershocks of the Iwate–Miyagi Nairiku earthquake obtained in the basin and mountain areas are used as the respective substitute EGFs.

Examples of the acceleration and velocity waveforms and the Fourier spectra obtained at AKTH06 from the after-

shock are shown in Figure 8. The displacement source spectra estimated using ground motion records at stations on rock are shown in Figure 9. The source spectra of the aftershock were obtained by removing the propagation-path effect and site effects from the observed spectra at the stations. The propagation-path effect is estimated using the spectral inversion method by Iwata and Irikura (1988), and then the site effects at the stations are empirically calculated, assuming that the source spectra are given by the ω^{-2} model and the propagation-path effect is given by frequency-dependent Q in propagation media (Tsurugi *et al.*, 1997). The corner

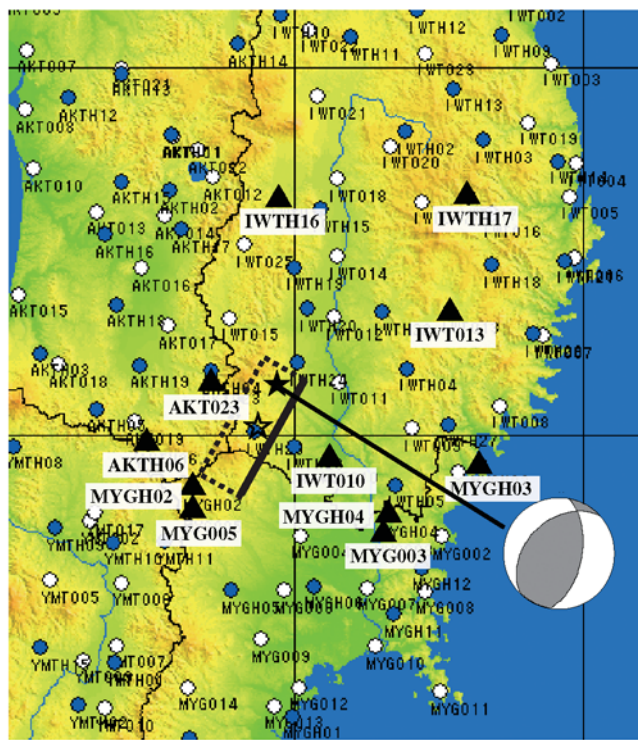


Figure 7. Map showing the source fault of the mainshock of the 2008 Iwate-Miyagi Nairiku earthquake in Japan (Suzuki *et al.*, 2008), the epicenters of the mainshock (open star symbol) and the aftershock (solid star symbol), and the locations of the stations used for analysis (solid triangle symbols). The focal mechanism of the aftershock determined by the F-net moment tensor inversion is shown at the bottom right. K-NET (open circle) and KiK-net (solid circle) stations are also shown, although they are not used in the present study.

frequencies of these spectra are determined by fitting the omega-square model. The source area of the aftershock is estimated from the corner frequency based on Brune's (1970; 1971) formula. The source information of the aftershock used as substitutes for the EGFs is listed in Table 2.

In order to reproduce the strong ground motions from the 2008 Wenchuan earthquake, we consider the source fault with a single segment, the southwestern segment. The source fault is assumed to be a characterized source model consisting of three asperities, according to the asperity locations shown in Figure 5a and b. Each asperity is divided into equal-sized square subfaults, the area of which is set to be the same as the aftershock area (i.e., $3.3 \times 3.3 \text{ km}^2$). The simulation of the earthquake is then performed at seven stations near the source fault of the earthquake, as shown in Figure 10. We selected the substitute EGFs for the stations considering the distances and radiation patterns from each asperity to the stations, as well as the ground conditions. The aftershock records used as the substitute EGFs at individual stations for each asperity are listed in Table 3. For example, the substitute EGFs at AXT for asperity 1 are the records obtained at IWTH17, and the substitute EGFs at WCW for asperity 2 are the records obtained at AKTH06 from the aftershock of the

2009 Iwate-Miyagi Nairiku earthquake. These aftershock records have sufficient accuracy at frequencies from 0.5 to 10 Hz. The spectra of the aftershock records show fluctuations at low frequencies less than 0.5 Hz (long periods more than 2 s), reflecting not source effects but surface waves in later phases generated from local geology, such as the basin and valley near the observation sites. Therefore, the observed records longer than 2 s are not always adequate as the substitutes of the EGFs for simulating ground motions for the Wenchuan earthquake.

Next, we simulated the ground motions for the characterized source model using the EGF method (Irikura, 1986). Our target is simulation of ground motions from the southwestern segment because the locations of asperities there are constrained by the backpropagation analysis in the previous section of this paper. We assumed that the strong ground motions are generated only from three asperities and not generated from the background area because we are concerned primarily with the acceleration and velocity motions, which are predominantly controlled by short-period motions from asperities. The best-fit characterized source model for simulating ground motions using the EGF method is determined by a trial-and-error approach, as shown in Figure 11, by comparing the observed and synthetic waveforms.

The observed and synthetic ground motions are shown in Figure 12. The agreement is satisfactory at most of the stations, including WCW, SFB, and MZQ, which are very near the source fault. The source parameters, such as the stress drop, the area, and the seismic moment of each asperity, used for the simulation are listed in Table 4.

Ground Motion Simulation by the Hybrid Method

Estimation of strong ground motions in the long-period range generated by a large earthquake has become possible as long as the source model and the velocity structures from source to site are known. However, propagation-path effects and site effects for strong ground motions in the short-period range are difficult to calculate numerically because of insufficient information concerning the velocity structures and source effects that is a result of limited knowledge concerning detailed rupture process. On the other hand, the observed records from small events have short-period motions that reflect the semiempirical characteristics of the propagation-path and local-site effects and the source effects. Then, hybrid methods for broadband strong ground motions of engineering interest have been developed by combining the numerical and EGF methods (e.g., Kamae *et al.*, 1998; Irikura and Kamae, 1999).

Simulation of Long-Period Motions Using Numerical Green's Functions

In the present study, long-period motions from the asperities are numerically calculated using the discrete wave-number (DWN) method for flat-layered structures (Bouchon,

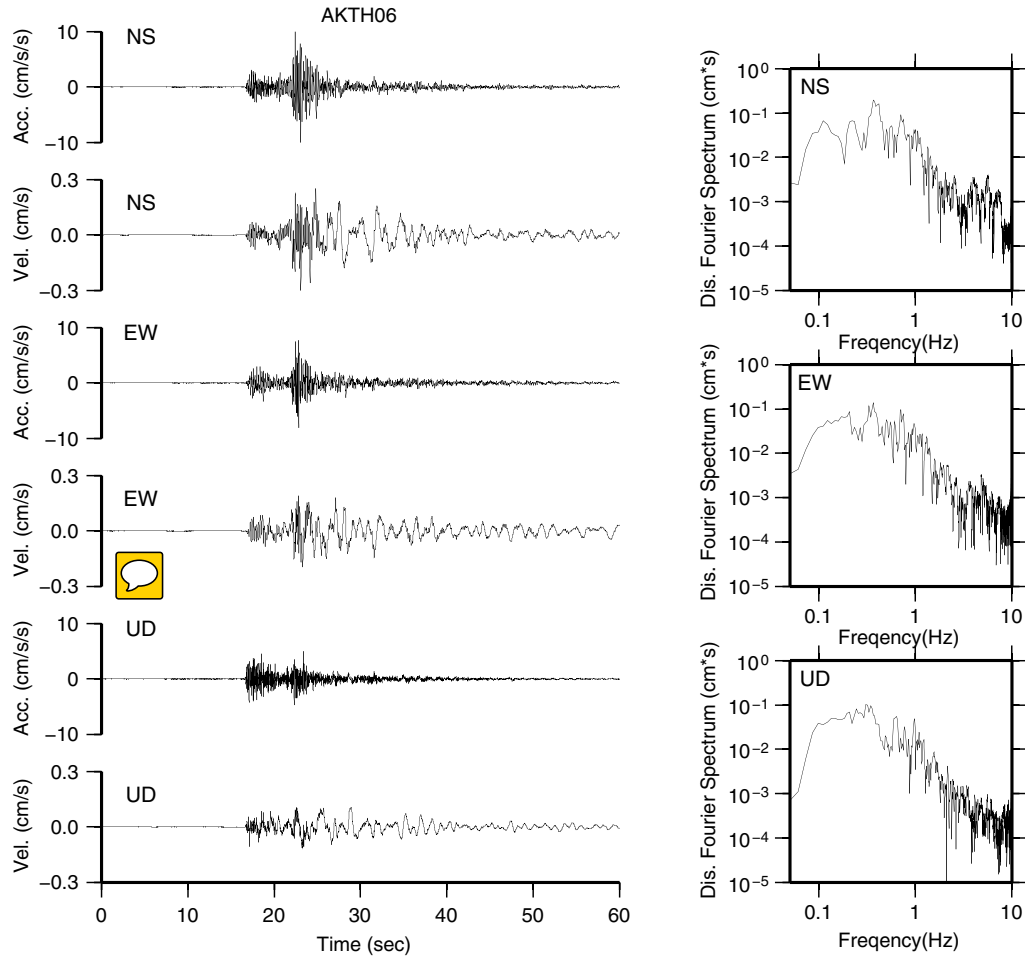


Figure 8. Examples of observed waveforms (horizontal north–south and east–west and vertical up–down components) and their Fourier spectra used as the empirical Green’s function at AKTH06.

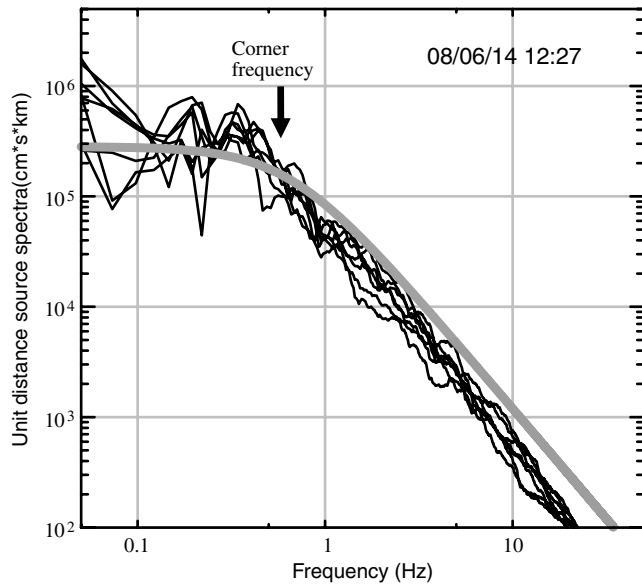


Figure 9. Displacement source spectra estimated using ground motion records at stations situated on rock. The corner frequency of these spectra is determined by fitting the omega-square model.

1981). The realistic velocity structures in the near-source area of the Wenchuan earthquake should be modeled as three-dimensional heterogeneous structures because they are located in the eastern margin of the Tibetan Plateau and the Sichuan basin (Wei *et al.*, 2008). Unfortunately, we have very limited information concerning the velocity structures in this area.

The *P*-wave and *S*-wave velocity and thickness of the shallowest layer were estimated from the structure model reported by Liu *et al.* (2009) for WCW, as shown in Figure 13a. They determined the velocity structures along the profile that crosses the fault zone of the Wenchuan earthquake, passing near WCW, using the nonlinear *P*-wave receiver function inversion technique. The *P*-wave and *S*-wave velocity and thickness of the shallowest layer for the other stations were estimated from that reported by Lou *et al.* (2008) and are shown in Figure 13b. They determined the velocity structures for the area northeast of the hypocenter using a joint analysis combining the receiver function method for the teleseismic *P*-wave receiver function method and Bouguer gravity anomalies. We assumed that the velocity structures for deeper layers have a simplified model with uniform *P*-wave and

Table 2

Source Parameters of an Aftershock of the 2008 Iwate–Miyagi Nairiku Used as the Empirical Green’s Functions

Origin time (dd/mm/yyyy, hr:min in JST)*	Latitude (deg)	Longitude (deg)	M_w	Stress Drop (MPa)	Area (km^2)	Strike	Dip	Rake
14/06/2008, 12:27	39.14	140.94	4.9	1.7	10.9	227	40	120

*JST, Japan Standard Time

S-wave velocity, although they were determined to have complex velocity structures by Liu *et al.* (2009) and Lou *et al.* (2008).

In order to simulate the long-period motions using the numerical method, we used the best-fit characterized source model obtained by the EGF method, as shown in Figure 11. As with the EGF method, the asperities are divided into equal-sized subfaults, the size of which is the aftershock area. For slip velocity time function for numerical simulation at each subfault, smoothed ramp function with rise time of 2 s is used. The synthetic velocity and displacement at WCW, SFB, MZQ, and AXT are compared with the observed ones in Figure 14. The agreement between the synthetic and observed velocity and displacement motions is satisfactory for the most part. However, a closer look at the synthetic waveforms at WCW reveals that the contributions from asperity 2, which is the largest asperity, are underestimated compared with the observed waveforms. The underestimation of ground motions at WCW in the backward direction of the rupture is discussed later in this paper. The large and long pulse seen in the east–west (EW) component at MZQ is not reproduced by the synthetic motion using the numerical Green’s functions (Figure 14). The reason is considered to be due to two factors. One is caused by the limitation of the velocity structure model and the other, by oversimplification

of the source model. We need further studies to solve this problem.

Simulation of Broadband Period Ground Motions using the Hybrid Method

The broadband period ground motions are calculated by summing the long-period motions ($T > 2$ s) numerically simulated by the DWN method (Bouchon, 1981) and the short-period ground motions ($T < 2$ s) simulated by the EGF method. A matched pair of filters consisting of low-pass (cut-off frequency: 0.5 Hz) and high-pass (cut-off frequency: 0.5 Hz) filters are used to smoothly combine the long-period and short-period motions.

The best source model is selected to minimize the residuals between the observed and synthetics defined by the following equation (Miyake *et al.*, 1999):

Residual values

$$\begin{aligned}
 &= \sum_{\text{station}} \sum_{\text{component}} \left[\sum_t (u_{\text{obs}} - u_{\text{syn}})^2 / \left\{ \left(\sum_t u_{\text{obs}}^2 \right) \right. \right. \\
 &\quad \times \left(\sum_t u_{\text{syn}}^2 \right) \left. \right\}^{1/2} + \sum_{\text{station}} (a_{\text{env,obs}} - a_{\text{env,syn}})^2 \\
 &\quad \left. \left. / \left(\sum_t a_{\text{env,obs}} \right) \left(\sum_t a_{\text{env,syn}} \right) \right] . \quad (6)
 \end{aligned}$$

The first and second terms mean the sum of squared residuals of displacement seismograms and that of acceleration envelopes, respectively.

The time window for calculating the residuals is set to be 10 s, including the pulses from asperity 2, the largest asperity. In this analysis, the area and stress drop of the asperity are fixed. The slip duration for simulating the ground motions from the asperity is changed with 0.5-s increments between 1 and 4 s. The evaluation function (6) is applied to simulated ground motions at SFB, MZQ, and AXT. Those at WCW in the backward direction are excluded because the simulated motions are more influenced by different parameters such as variances of rupture velocities and rupture patterns. The residuals were found to be minimized for the slip duration of 2.0 s. The waveforms of the observed and synthetic ground motions for the best-fit characterized source model are shown in Figure 15, and acceleration response spectra (Sa) and pseudovelocility spectra (pSv) ($h = 5\%$) of them are shown in Figure 16. Except for the east–west motions at MZQ, the agreement is satisfactory at most of the stations, including SFB, AXT, and MZQ.

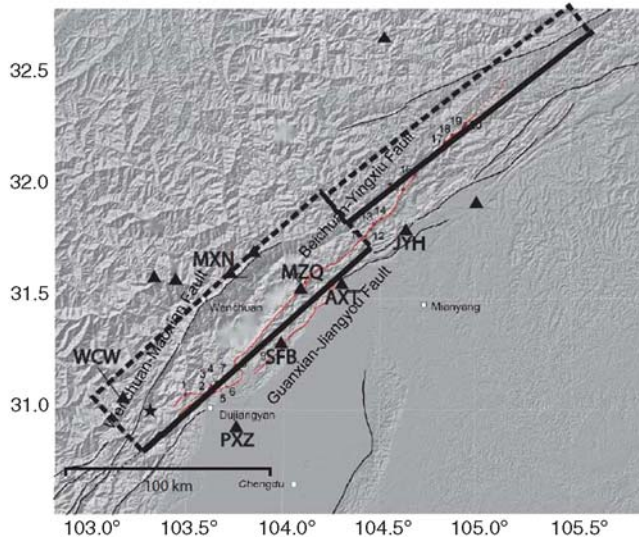


Figure 10. Map showing the source fault, consisting of two segments for the mainshock of the Wenchuan earthquake reported by Koketsu *et al.* (2009). The star symbol shows the epicenter of the mainshock, and the triangle symbols indicate the strong-motion stations. The base map is from Ikeda *et al.* (2008).

Table 3

List of Stations at which Ground Motion Records Were Used as the Empirical Green's Functions*

Station	Hypocentral Distance	Epicentral Distance	Azimuth	Station	Hypocentral Distance	Epicentral Distance	Azimuth
Asperity 1							
AXT	113.4	112.5	56.7	IWTH17	80.0	79.2	45.5
JYH	154.0	153.3	54.6	IWTH17	80.0	79.2	45.5
MZQ	96.0	95.0	51.2	IWTH17	80.0	79.2	45.5
PXZ	46.0	43.8	101.0	MYGH03	66.3	65.4	112.1
SFB	73.9	72.6	63.1	IWTH17	80.0	79.2	45.5
WCW	19.6	13.8	295.8	AKT023	22.1	19.2	270.2
MXN	78.3	77.0	31.2	IWTH17	80.0	79.2	45.5
Asperity 2							
AXT	73.8	72.4	55.1	IWT013	56.9	55.8	67.5
JYH	114.2	113.4	52.9	IWT013	56.9	55.8	67.5
MZQ	57.3	55.6	45.2	IWT013	56.9	55.8	67.5
PXZ	32.8	29.7	164.1	IWT010	30.2	28.2	146.8
SFB	35.4	32.5	67.3	IWT013	56.9	55.8	67.5
WCW	51.2	49.3	253.5	AKTH06	44.0	42.6	244.6
MXN	48.1	46.0	6.5	IWTH16	56.3	55.3	0.6
Asperity 3							
AXT	51.2	44.2	107.4	MYG003	56.9	55.8	144.7
JYH	78.9	74.6	79.6	IWTH17	80.0	79.2	45.5
MZQ	37.5	27.1	124.9	MYGH04	53.2	52.8	140.0
PXZ	87.6	82.7	186.3	MYGH02	41.9	40.5	218.2
SFB	51.1	44.0	163.0	MYGH04	53.2	52.8	140.0
WCW	97.6	94.1	233.3	MYG005	47.2	45.9	213.1
MXN	29.9	14.9	237.3	AKTH06	44.0	42.6	244.6

*The selected stations were similar to the stations at which ground motions from the 2008 Wenchuan earthquake were observed with respect to epicentral and hypocentral distance and azimuthal angle.

Looking at the synthetic results in detail, in particular the vertical motions, the ground motions at SFB have clearly larger amplitude than the observed ones. Distinctive pulses

seen in the synthetic motions are due to rupture directivity pulses, which appear at sites in the forward rupture direction and very close to asperity 2, the largest asperity. On the other hand, the ground motions at WCW in the backward direction to asperity 2 have smaller amplitudes compared with the observed. It is important why the synthetic motions have excessive directive pulses in the forward rupture direction. This might be one of the disadvantages in applying the characterized source model to strong-motion prediction. We later note in the Discussion section how to avoid too strong directivity effects.

The simulated ground motions of the east–west component at MZQ show smaller amplitudes than the observed ones. Further studies are necessary from the viewpoints of source modeling, such as near-field term and fringe effects and structure modeling such as three-dimensional structural effects to ground motions.

Discussion

In the present study, three problems remain to discuss here: First are the strong directivity effects in the forward rupture direction and the influence of rupture-velocity fluctuation on synthetic motions; second is the influence of slips in background area on synthetic motions; and third is the validity of the recipe for strong-motion prediction.

We begin with examining the reasons why such strong directivity pulses in the synthetic motions at SFB from

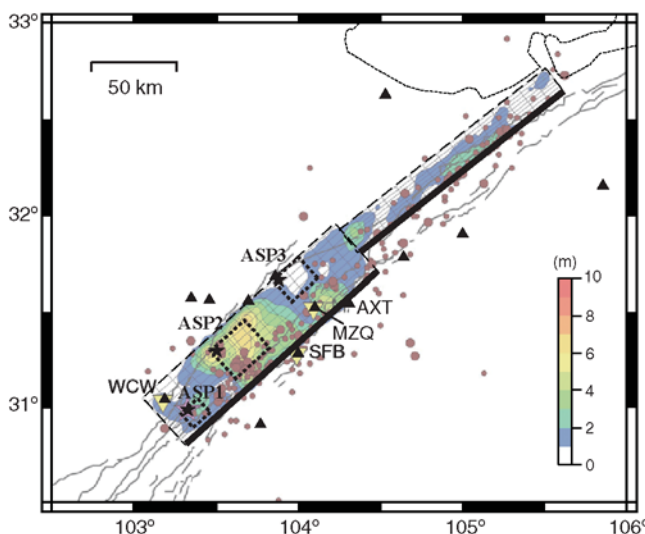


Figure 11. Source model consisting of three asperities on the northern segment. The area and stress drop on each asperity were estimated from the forward modeling using the empirical Green's function method. The three asperities (rectangles) are overwritten on the slip distribution obtained by Koketsu *et al.* (2009). The triangle symbols indicate the locations of strong-motion stations used for simulation by the empirical Green's function method.

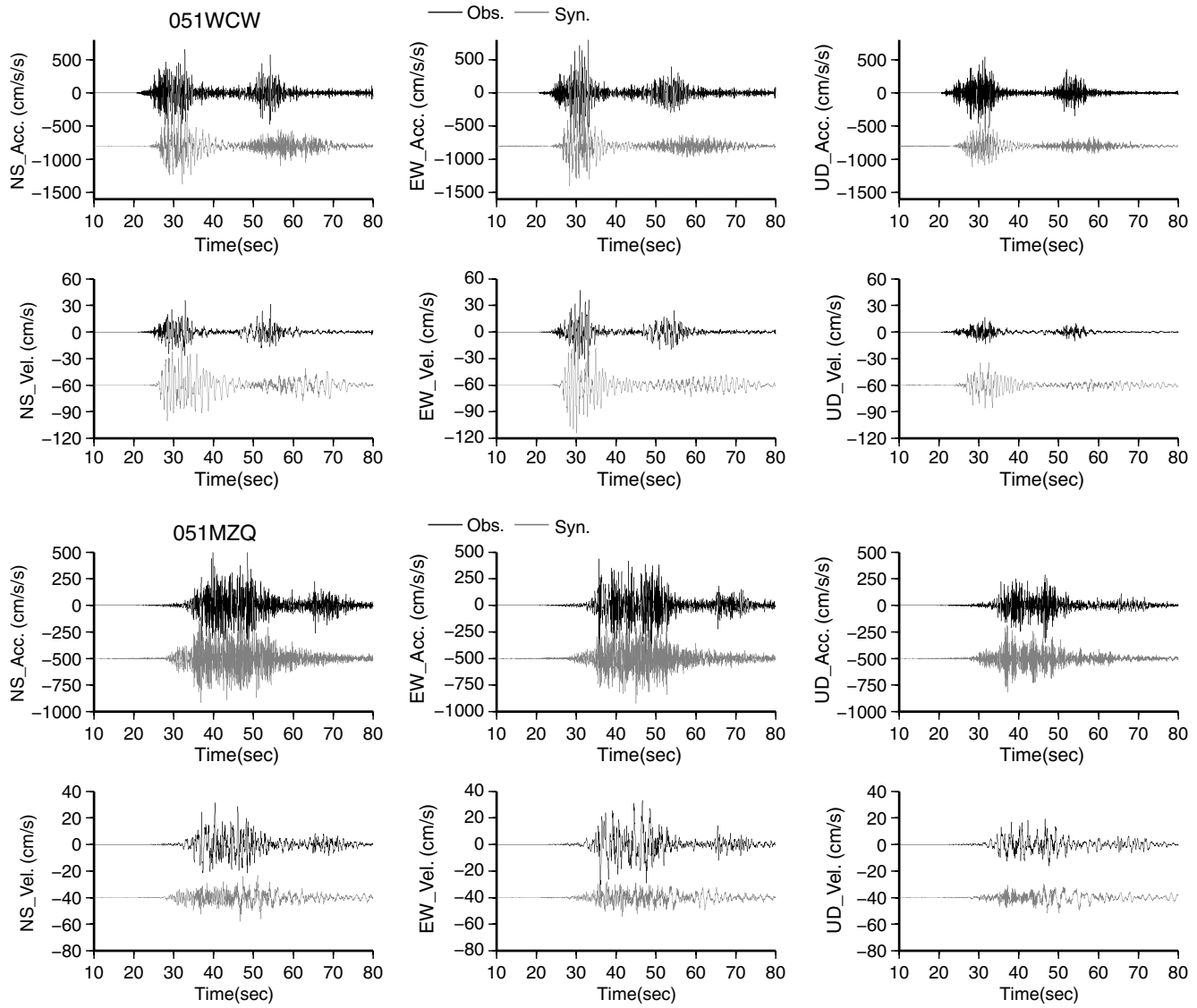


Figure 12. Comparison of the observed and synthesized waveforms by the empirical Green's function method at WCW, SFB, MZQ, and AXT. The acceleration (top), and velocity (bottom) at each station are shown. The period range available for simulation is from 0.1 to 2.0 s. The observed motions are also band-pass-filtered in the same period range. (Continued)

asperity 2 appear. One is the effects of mesh-sizes on the synthetic ground motions as a technical artifact. The other is the influence of constant velocity of rupture and constant rake angle of slip in an asperity on the synthetic ones. In the EGF method, each asperity is divided into $N \times N$ subfaults. The subfault has area with $3.3 \times 3.3 \text{ km}^2$, consistent to the size of the small event used as the EGF. In our numerical simulation we adopt the same subfault size. Each subfault is assumed to be a point source with a certain seismic moment. Rupture propagation inside each subfault in the present numerical simulation is neglected. The EGF method uses the observed records from small events that include the source information concerning the rupture propagation inside the small event fault. To numerically simulate rupture propagation inside the subfault, finer meshes are necessary in the subfault.

We examine the effects of the subfault size on ground motions from asperity 2 for the following three cases. The mesh size is $3.3 \times 3.3 \text{ km}^2$ in case A; $1.1 \times 1.1 \text{ km}^2$ in case B, subdividing the subfault in case A into 3×3 elements; and $0.55 \times 0.55 \text{ km}^2$ in case C, subdividing the subfault in case A into 6×6 elements. The synthetic ground motions at SFB for source models with different mesh size are compared in Figure 17. The amplitudes of the directivity pulse for the source models in case B and case C divided into finer meshes are clearly reduced compared with those for case A, while those are almost the same for case B and case C. The strong directivity effects seen in the synthetic motions for case A at SFB partly are due to the influence of the mesh size.

Another problem is related to constant velocity of rupture. The influence of the turbulence in the rupture front on

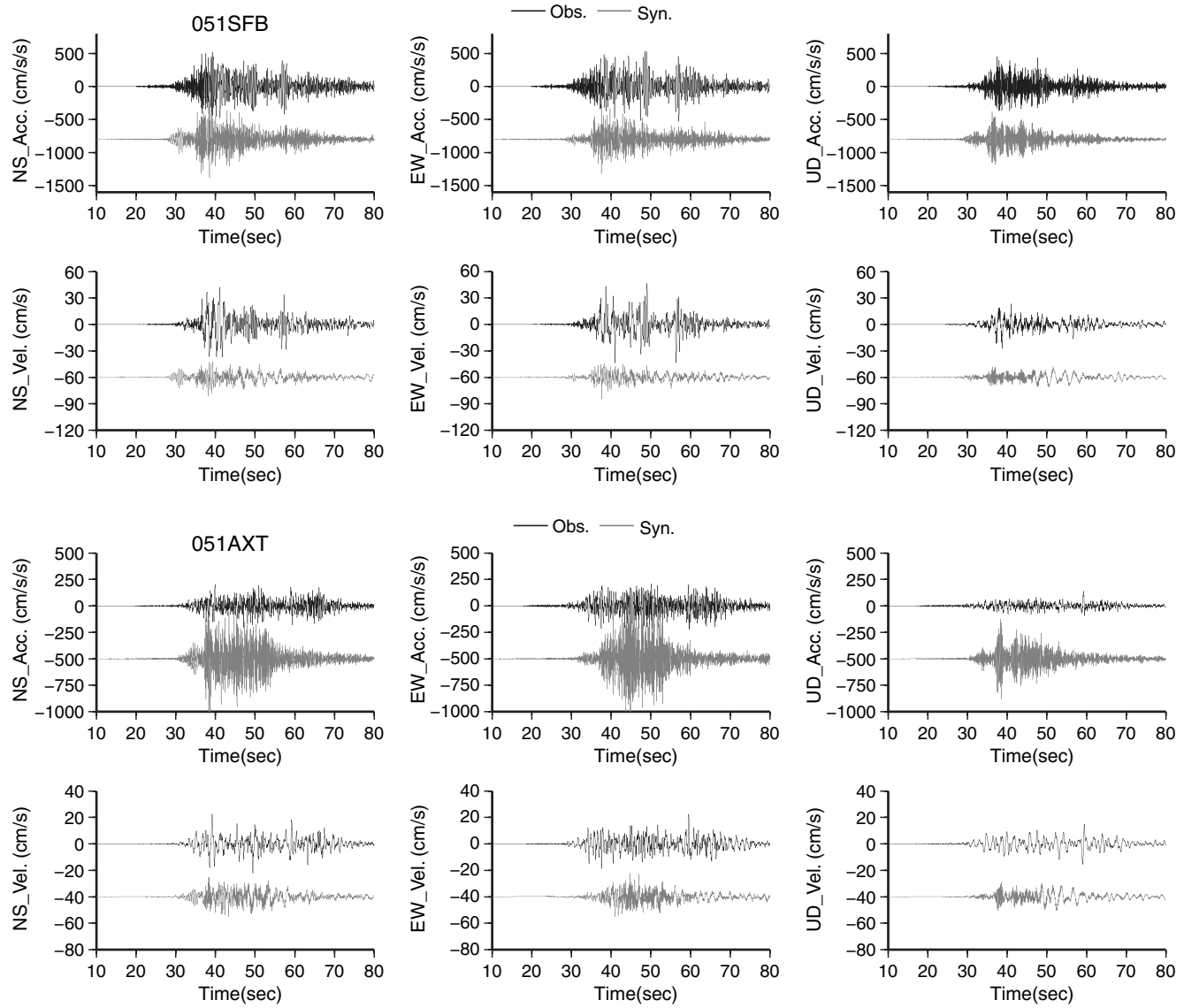


Figure 12. Continued.

simulated ground motions has been indicated by Hisada (2006) and Watanabe *et al.* (2008). In order to improve the overestimation of the directivity pulse in the forward rupture direction, we examine the influence of rupture-velocity fluctuation on synthetic motions at SFB for the finer-meshed model (case B in Fig. 17). Three cases of the rupture-velocity fluctuation are tested. The rupture velocity over the asperity remains constant in case 1, which is the same as the model in

Table 4
Source Parameters of the Three Asperities

	Area (km ²)	M_0 (N m)	Stress Drop (MPa)
Asp1	174.2	1.38E+19	13.6
Asp2	696.7	1.11E+20	13.6
Asp3	392.0	4.67E+19	13.6

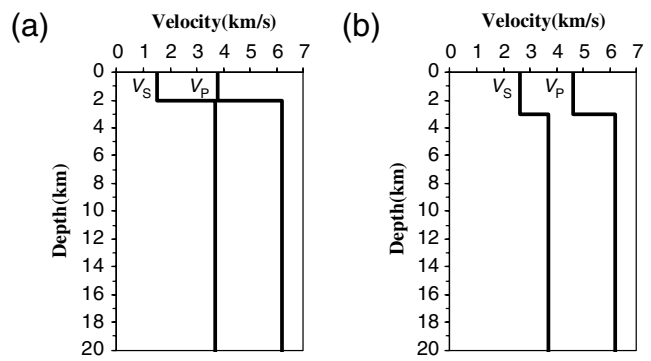


Figure 13. P- and S-wave velocity structure models (a) at WCW and (b) at the other stations. The velocity models are estimated, based on (a) Liu *et al.* (2009) and (b) Lou *et al.* (2008).

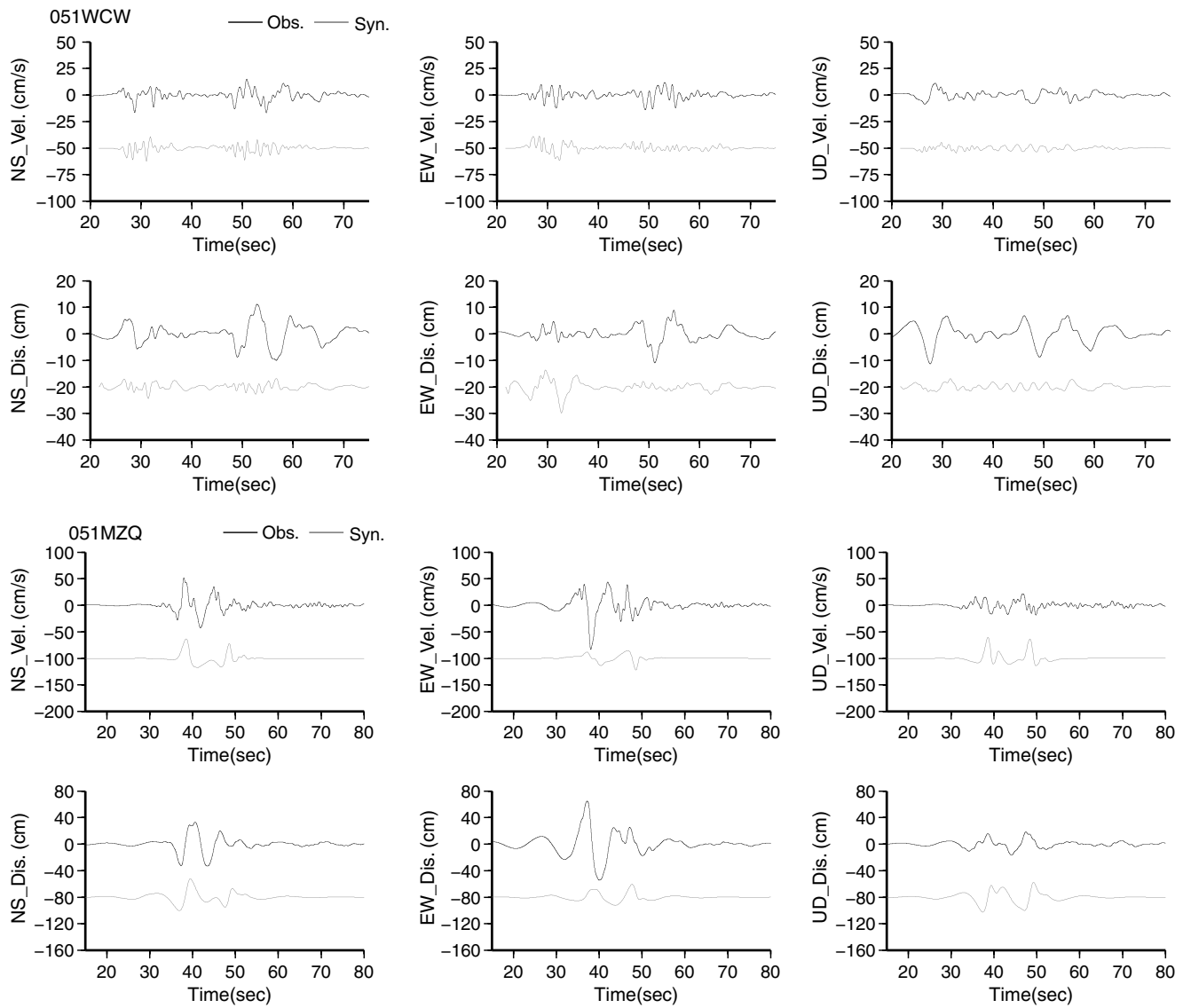


Figure 14. Comparison of the observed and synthetic waveforms numerically calculated by the discrete wavenumber method.

(Continued)

Figure 11. The rupture velocity over the asperity fluctuates by random numbers distributed uniformly in the range of 10% of mean velocity in case 2 and 20% in case 3. The amplitudes of the contributions from asperity 2 to the synthetic waveforms decrease at SFB in the forward rupture direction area, as the rupture velocity over the asperity fluctuates. The amplitude–frequency distribution for cases 2 and 3 are shown in Figure 18. The growth rate in Figure 18 is defined to be the ratio of the maximum amplitudes of the synthetic motions with velocity variance to those with constant velocity. The maximum amplitudes of the synthetic waveforms from asperity 2 become smaller on average with the increase in the velocity variance, although the maximum amplitudes fluctuate in each trial. The median decrease rates for the rupture-velocity variances of 10% and 20% are approximately 0.8 and 0.6, respectively.

The synthetic waveforms for case 1 and case 2 are compared with the observed ones in Figure 19a and b, respectively, where the source model of case 2 is one of the models with 10% rupture-velocity variance, having the median maximum amplitudes. We find that the synthetic waveforms for case 2 are in better agreement with the observed waveforms. This means that some fluctuations of the rupture velocity should be introduced in simulating ground motions in the forward rupture areas.

We also examine the influence of the rupture-velocity fluctuation on the synthetic waveforms at WCW in the backward rupture direction area. The maximum amplitudes of the synthetic waveforms at WCW in case 2 and case 3 increase compared with those in case 1. However, the synthetic waveforms in the backward rupture direction are still smaller than the observed. We need to consider the influence of

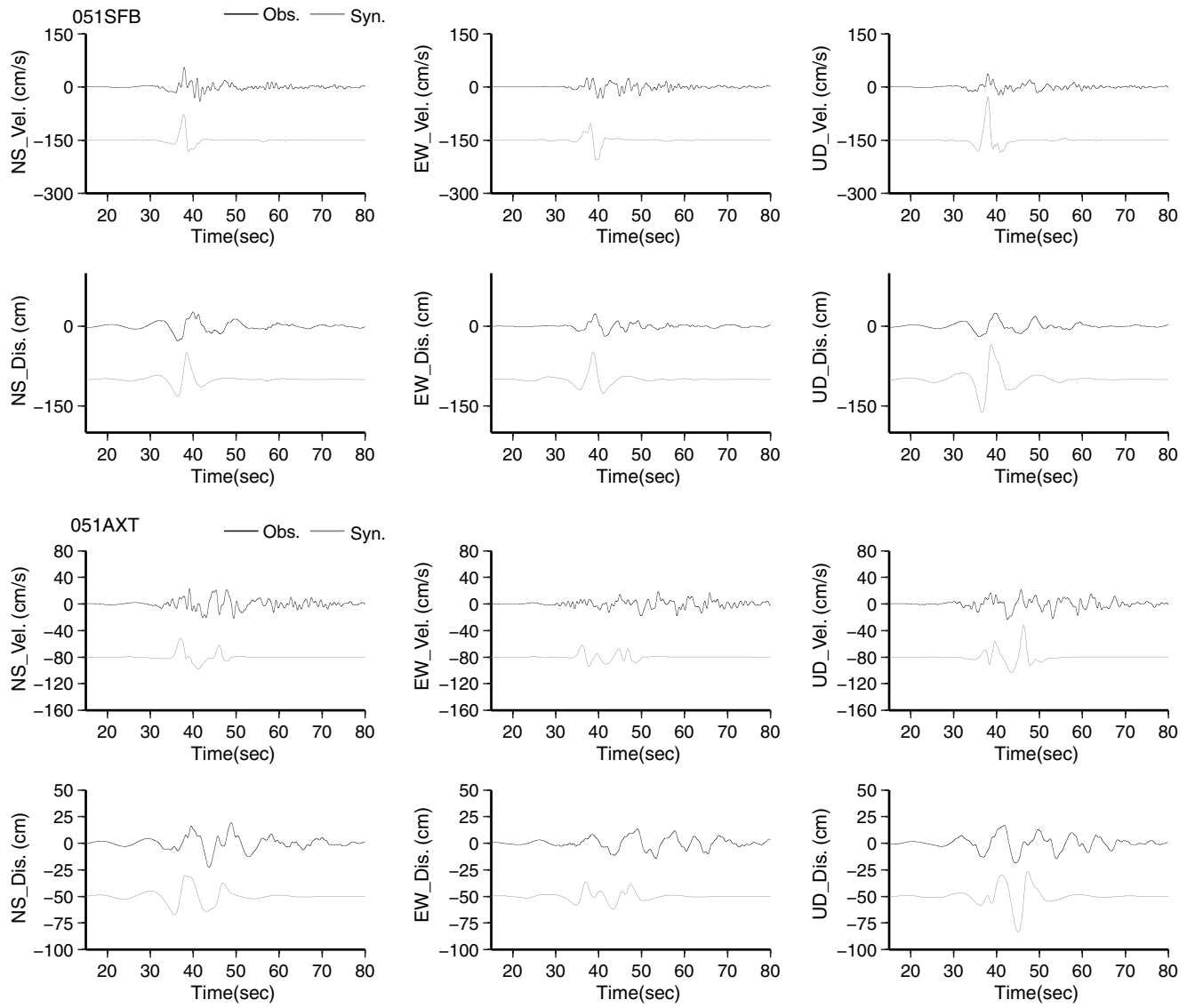


Figure 14. Continued.

other factors on ground motions at WCW (e.g., the three-dimensional structure model from the source area to the station).

The second concern is the influence of slips in the background area of the source fault on synthetic motions. Thus far, we calculated the contributions from only the asperities to ground motions, neglecting the contributions from the background areas. According to Somerville *et al.* (1999), the seismic moment release from the combined areas of the asperities is approximately 44% of the total seismic moment. We evaluate the influence of the slips in the background areas on the synthetic motions in this study. The seismic moment of this earthquake is 1.0×10^{21} N m (from Koketsu *et al.*, 2009), including the southern and northern segments. The seismic moment released from all of the asperities in the northern segments is 1.72×10^{20} N m. The seismic moment of the southern segment is assumed to be

half of the total seismic moment because it was not shown in the reference. The slip and stress drop in the background area are estimated from the seismic moment given as the total seismic moment released from the southern segment minus the seismic moment of the asperities. The background area is also divided into equal-sized subfaults, the size of which is 3.3×3.3 km 2 .

At WCW, synthetic motions from the asperities are very small, in particular the motions from asperity 2 in comparison with the observed records because WCW is located in the backward rupture direction. The upper graphs in Figure 20 show ground motions numerically simulated from all of the asperities and those from the background areas to the ground motions at WCW, respectively. The contributions of the background area to ground motions at WCW have smaller amplitudes than those of the asperities as shown in the top of Figure 20. Underestimation of the

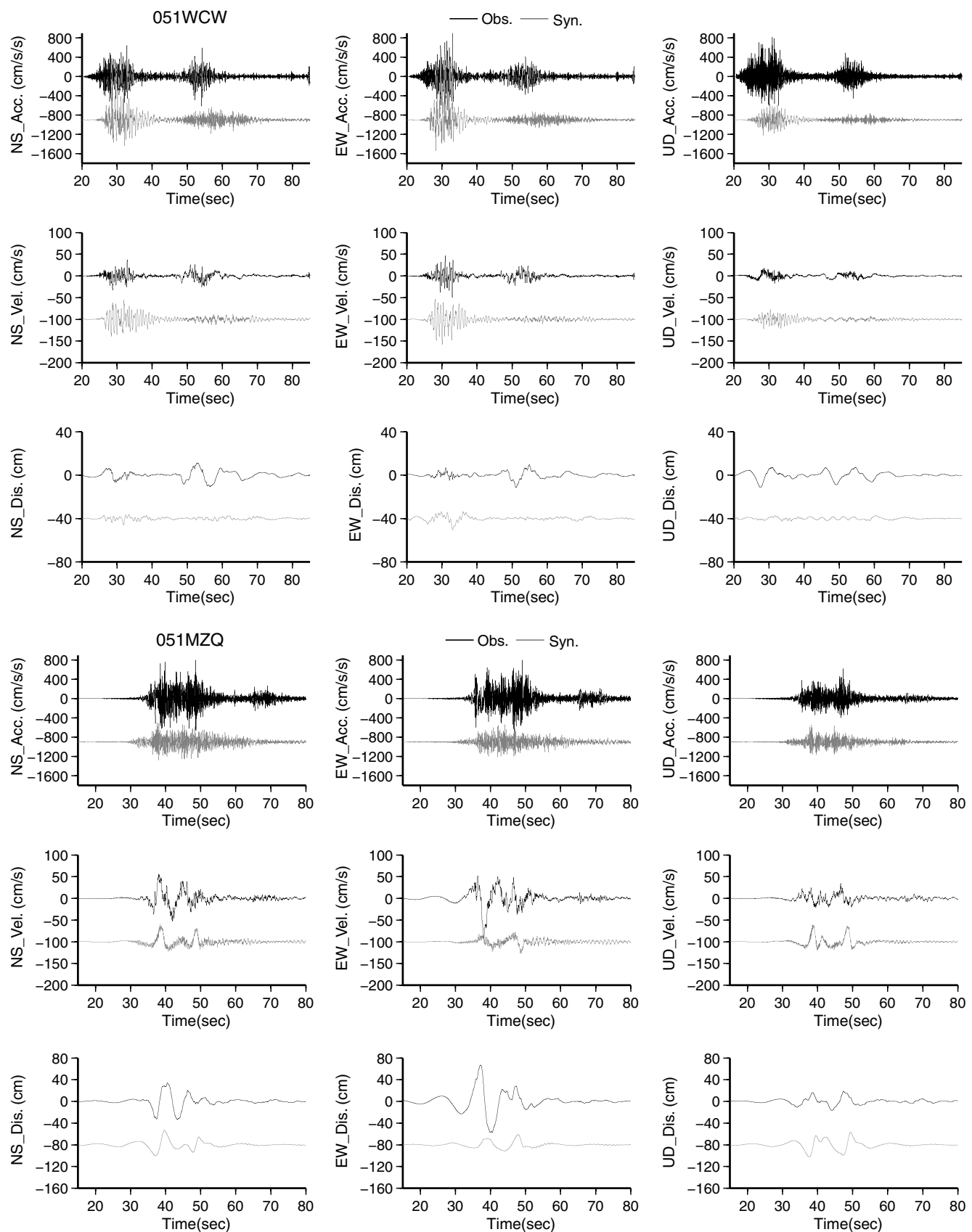


Figure 15 Comparison of the observed and synthetic waveforms simulated by the hybrid method for the best-fit characterized source model. (Continued)

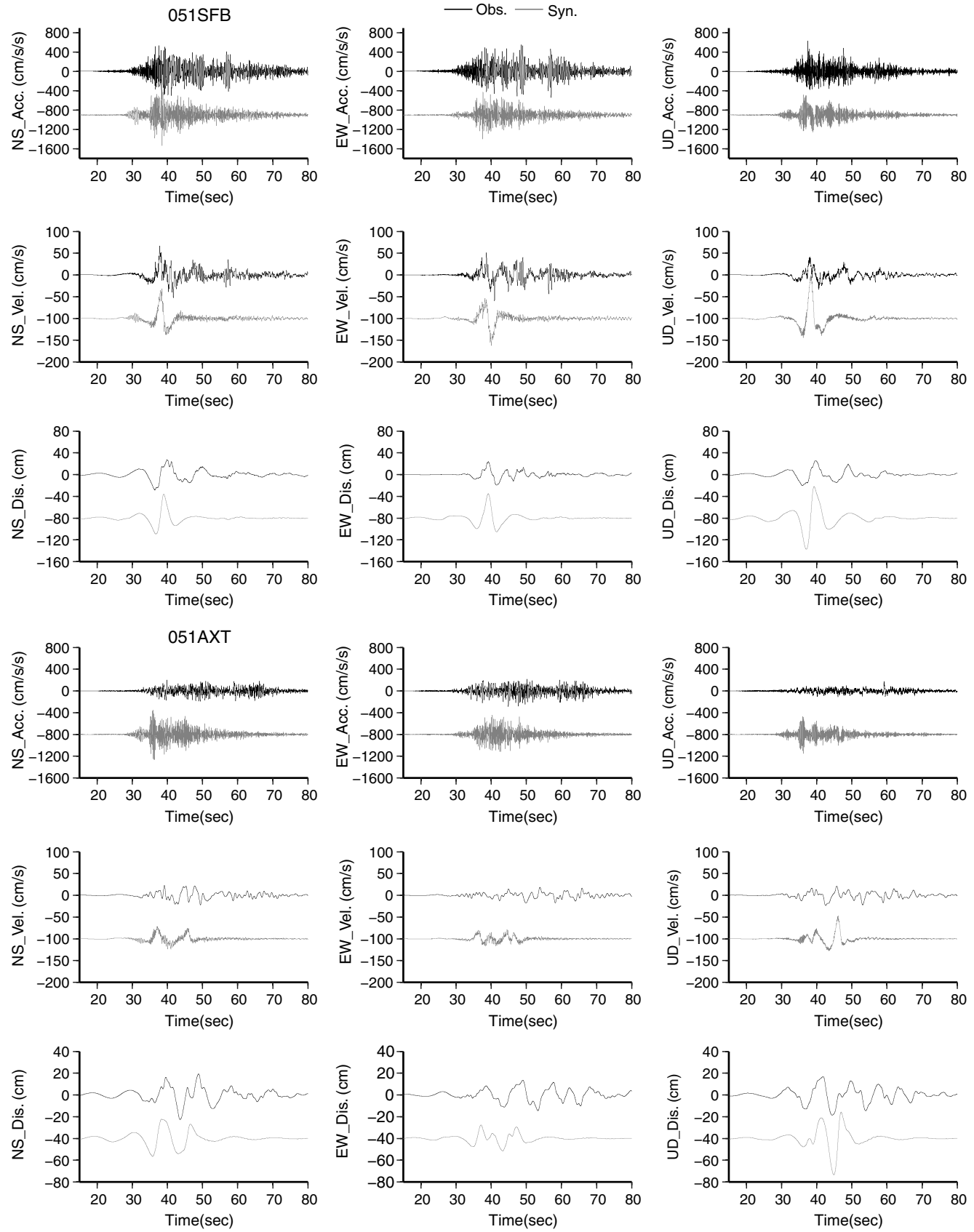


Figure 15 Continued.

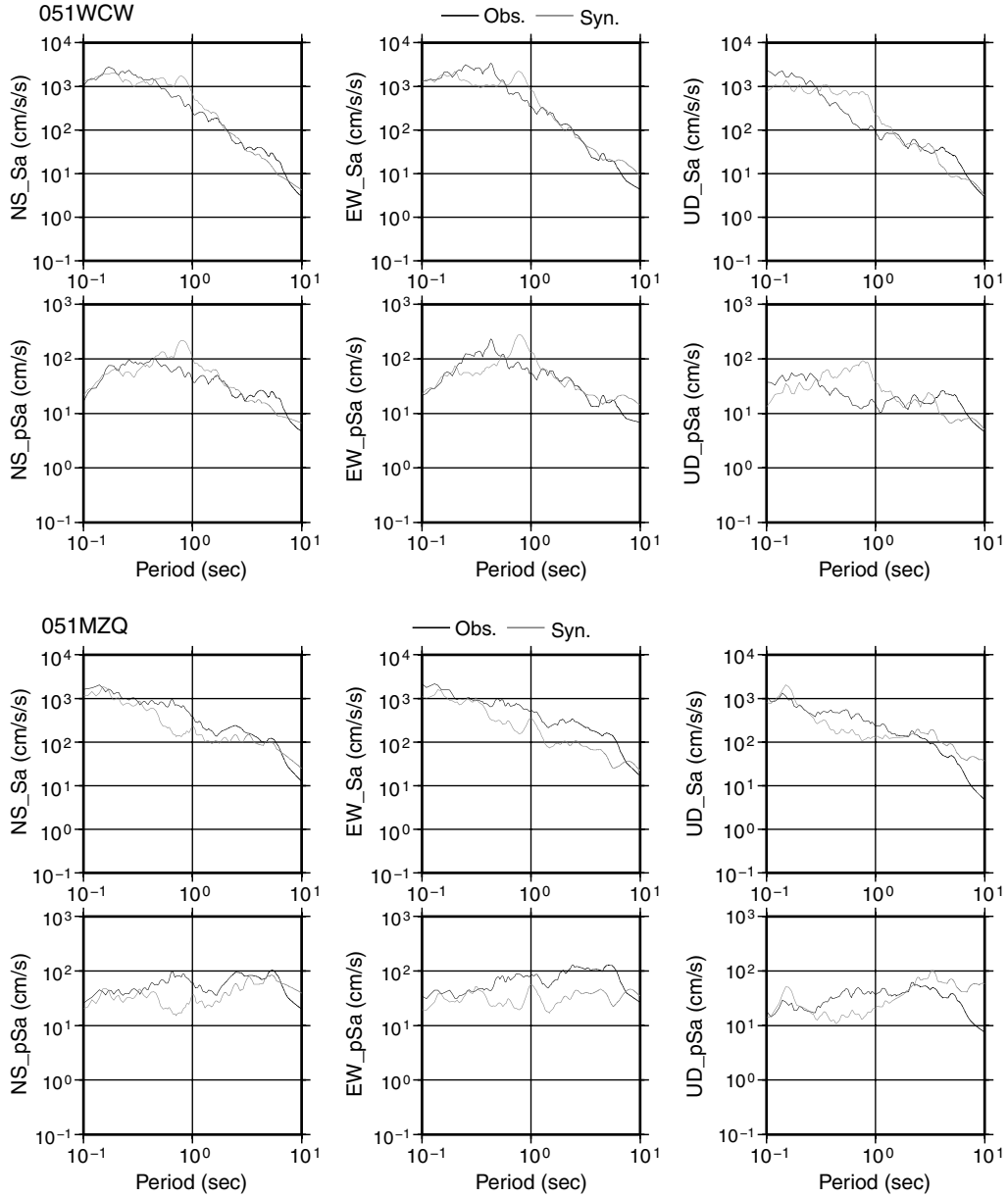


Figure 16. Comparison between acceleration response spectra (Sa) and pseudo velocity spectra (pSv) ($h = 5\%$) of the observed ones and those of the synthetic calculated by the hybrid method for the best-fit characterized source model. *(Continued)*

simulated ground motions at WCW are not attributed to the slip occurring outside of the asperities in the period range from 0.1 to 10 s.

The third concern is to discuss the validity of the recipe for strong-motion prediction. A recipe for predicting strong ground motions has been developed based on the characterized source model for future crustal earthquakes (Irikura and Miyake, 2001; Irikura and Miyake, 2010). The source parameters for characterizing the source model are given for the scaling relationships of the outer fault parameters and the inner fault parameters. The outer fault parameters are given from the empirical relationship between the entire rupture area and the total seismic moment. The inner fault pa-

rameters are given from the empirical relationship between the entire rupture area and the combined areas of the asperities. From these relationships, the stress drop on the asperities $\Delta\sigma_a$ is given by Madariaga (1979) as

$$\Delta\sigma_a = \Delta\bar{\sigma}_c \cdot \frac{S}{S_a}, \quad (7)$$

where S , S_a , and $\Delta\bar{\sigma}_c$ are the entire rupture area, the asperity area, and the average stress drop over the entire rupture area. The asperity areas and the stress drop on the asperities are two of the most important parameters for estimating the waveform shapes of ground motions from specific faults.

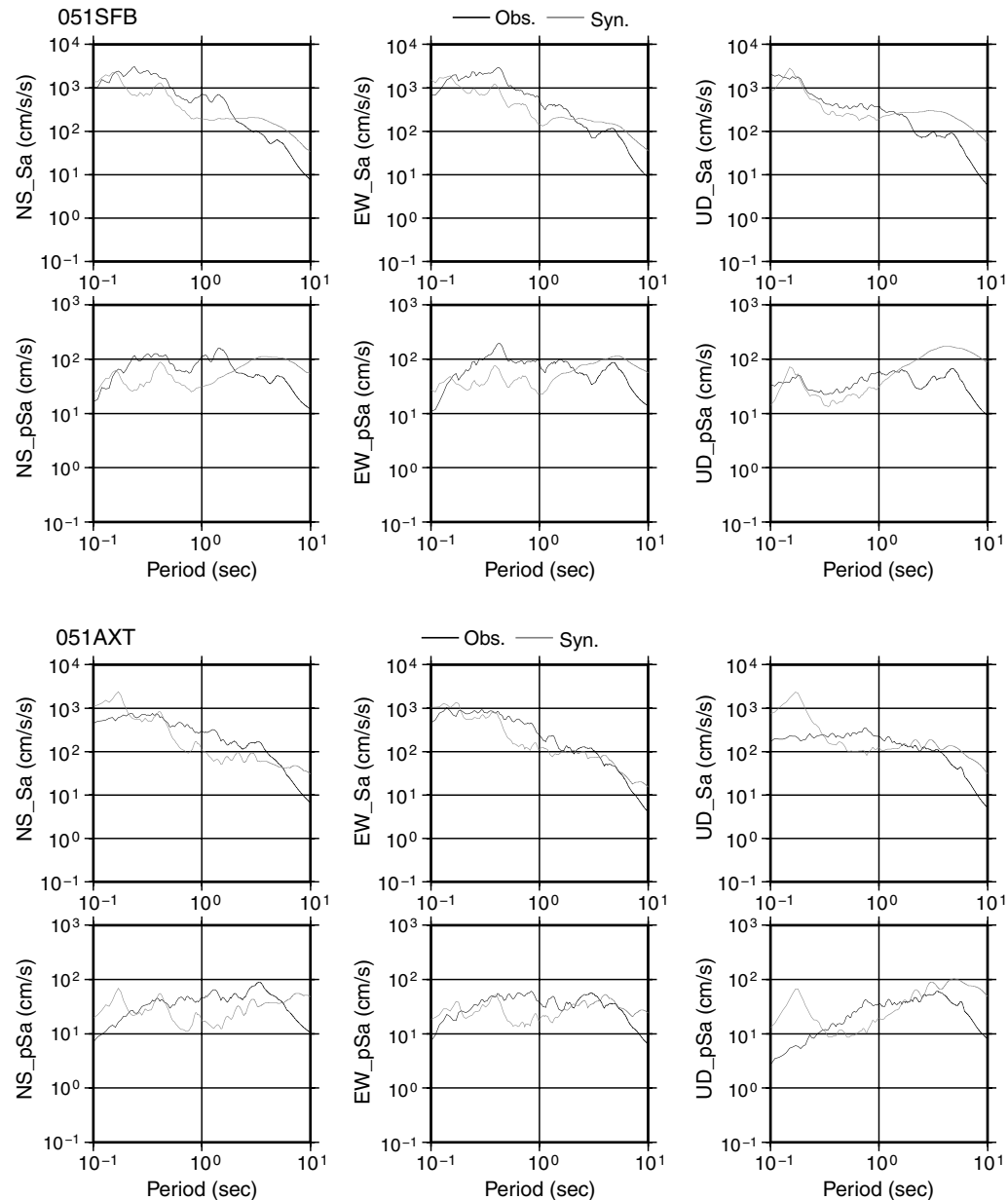


Figure 16. Continued.

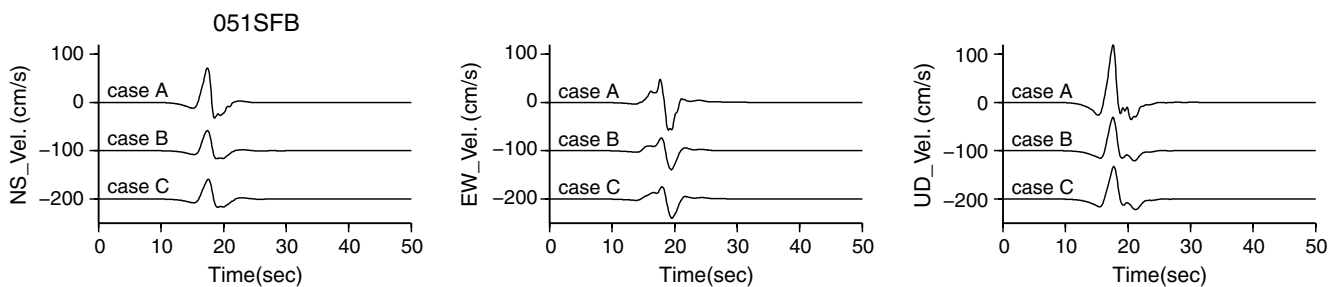


Figure 17. The synthetic ground motions at SFB numerically calculated for source models with different mesh size. Case A: mesh of $3.3 \times 3.3 \text{ km}^2$. Case B: mesh of $1.1 \times 1.1 \text{ km}^2$. Case C: $0.55 \times 0.55 \text{ km}^2$.

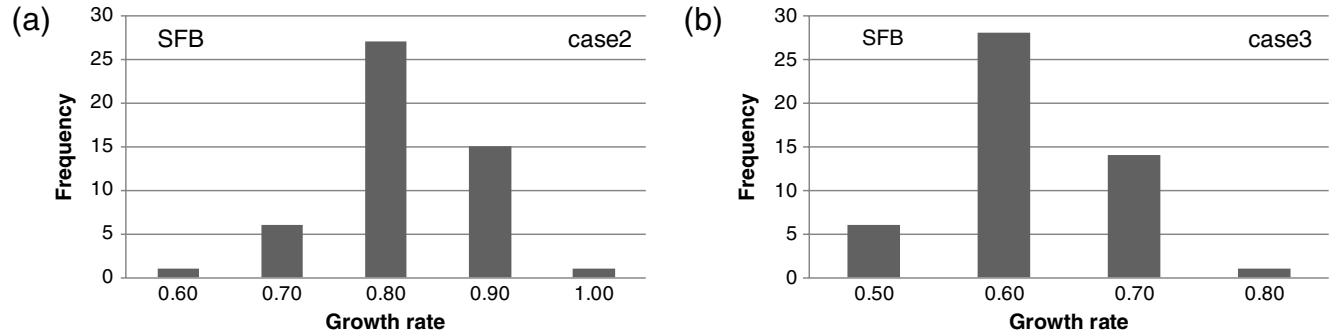


Figure 18. Amplitude–frequency distributions for (a) case 2 (rupture velocity with a 10% variance) and (b) case 3 (rupture velocity with a 20% variance). The growth rate is defined as the ratio of the maximum amplitudes of the synthetic motions with velocity variance to the maximum amplitudes of the synthetic waveforms of the north–south (NS) component from asperity 2.

We have examined the validity of the earthquake sources constructed by the proposed recipe by comparing simulated and observed ground motions from recent inland crustal earthquakes, such as the 1995 Kobe and 2005 Fukuoka earthquakes (Irikura and Miyake, 2010). Ground motions from these earthquakes are found to be predictable as long as the source faults are specified through investigation of active folds and faults.

We validate that the outer and inner fault parameters of the Wenchuan earthquake follow the scaling relationships obtained thus far. The relationship between the seismic moment and rupture area for inland crustal earthquakes, including the Wenchuan earthquake, is summarized as shown in Figure 21 (Irikura, 2004; Koketsu *et al.*, 2009). For earthquakes with a seismic moment greater than 1.0×10^{19} N m, the scaling tends to depart from the self-similar model (Irikura and Miyake, 2001). This departure corresponds to the saturation of the fault width in a finite-size seismogenic zone. Such a two-stage scaling relationship was also reported by Hanks and Bakun (2002). However, earthquakes for a low-angle reverse fault, such as the 1999 Chi-Chi earthquake, seem to maintain the self-similar relation reported by Somerville *et al.* (1999) without deviation. The Wenchuan earthquake appears to have the tendency of a low-angle reverse fault.

The empirical relationship between the rupture area S and the combined area of asperities is shown in Figure 22, adding the Wenchuan earthquake to Irikura and Miyake (2001). The rupture area S and combined area of asperities S_a of the Wenchuan earthquake are plotted for the southwestern segment in Figure 2b, because the present analysis is available only for the southwestern segment. The ratio S_a/S for the Wenchuan earthquake appears to follow the empirical relationship, with a value of approximately 0.22 for inland earthquakes. Source modeling based on the proposed recipe appears to be useful for magnitude-8 mega earthquakes, such as the Wenchuan earthquake.

Conclusions

We estimate the characterized source model for simulating ground motions during the 2008 Wenchuan earthquake.

Based on the joint inversion of the teleseismic and strong-motion data by Koketsu *et al.* (2009), the characterized source model consists of three asperities with large slip in the southwestern segment of the source fault. The locations of the three asperities that generate strong motions were determined from the timing of pulse arrivals appearing in the observed waveforms near the source fault.

We first tried to simulate strong ground motions from the earthquake using the EGF method. Because there were no aftershock records of the Wenchuan earthquake, we used ground motion records from small events that had occurred in other regions in place of the EGFs. For the EGFs, it is necessary to select small event records for which (1) the source mechanism associated with the source effect, (2) the hypocentral distance related to the propagation-path effects, and (3) the surface geology related to the site effects are similar to those of the target event.

Therefore, as the substitute EGF method, we selected the observed records from an aftershock (M_w 4.9) of the 2008 Iwate–Miyagi Nairiku earthquake (M_w 6.9) that occurred in the shallow inland crust of the northeastern region in Japan. We then obtained the best-fit characterized source model with appropriate areas of the asperities and stress drops on the asperities by trial and error, by comparing the observed records and synthetic motions. The synthetic motions obtained by the EGF method agree well with the observed motions in acceleration and velocity waveforms in the period range of less than 2 s. The stress drop on each asperity is assumed to be approximately 13 MPa for the best-fit source model.

Next, broader-band strong motions are simulated by the hybrid method that combines the numerical method for periods longer than 2 s and the EGF method for periods shorter than 2 s. The long-period ground motions are generally well simulated at the stations in the forward direction for the asperities, but those in the backward rupture direction for the asperities are underestimated as compared with the observed motions. In detail, synthetic motions at SFB very close to asperity 2 and in the forward rupture direction have too strong directivity effects compared with observed records.

To improve the overestimation of ground motions due to the forward directivity, the influence of the rupture-velocity

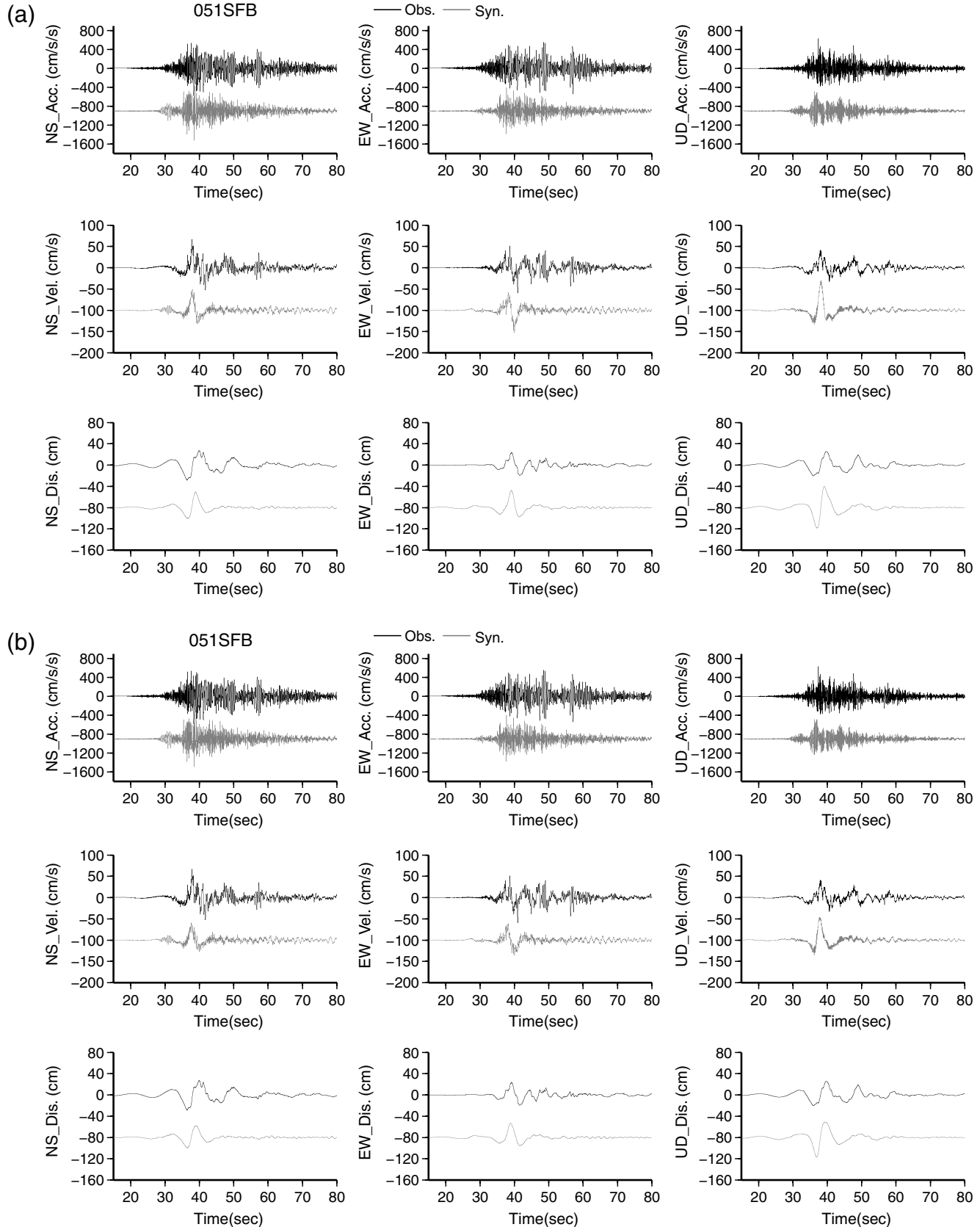


Figure 19. Comparison between the observed and synthesized velocity motions at SFB simulated by the hybrid method. (a) Case 1 (constant rupture velocity). (b) Case 2 (rupture velocity with a 10% variance).

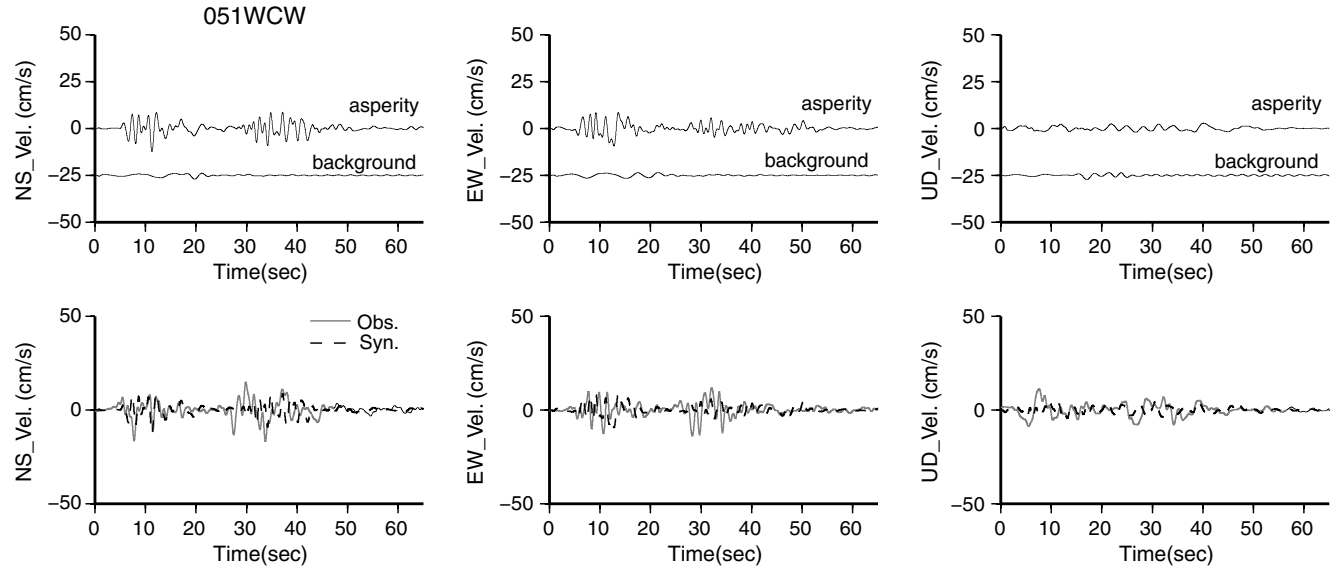


Figure 20. Comparison of velocity motions for asperities and those for background area at WCW. In the upper graphs, ground motions numerically simulated for all of the asperities and those for the background areas are compared, respectively. The synthetic ground motions for both combined asperities and background area are compared with the observed records in the bottom panel.

fluctuations on the synthesized waveforms is examined by means of the variance of rupture velocity over the largest asperity. The mean maximum amplitudes of the synthetic waveforms from asperity 2 are found to become smaller as the velocity variances increase, although the maximum amplitudes fluctuate in each trial. The medians of the growth rates for the rupture-velocity variances of 10% and 20% are approximately 0.8 and 0.6, respectively. The synthetic waveforms with 10% variance of rupture velocity (2.9 cm/s) show very good agreement with the observed waveforms.

Finally, the combined area S_a of the asperities of the present model were compared with the rupture area S for the southwestern segment. The ratio S_a/S for the Wenchuan

earthquake was found to follow the empirical relationship used as the recipe for predicting strong ground motions with a value of approximately 0.22 for inland earthquakes (Irikura and Miyake, 2001). The source modeling based on the proposed recipe is applicable to magnitude-8 mega earthquakes, such as the Wenchuan earthquake.

Data and Resources

The moment magnitude and the location of the hypocenter used in this study were provided by the U.S. Geological Survey (<http://earthquake.usgs.gov/earthquakes/eqinthenews/2008/us2008ryan/>; last accessed September 2010). The

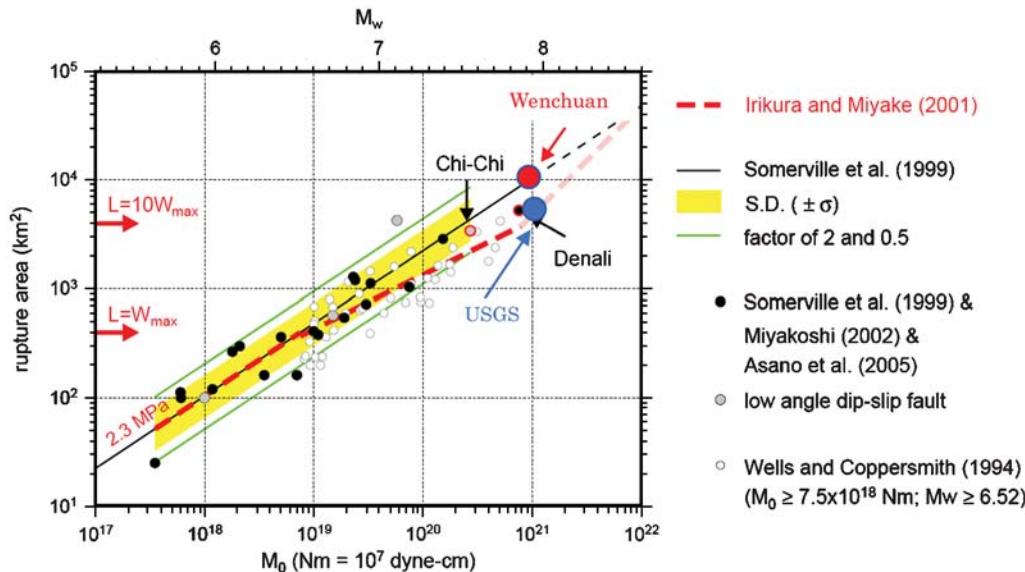


Figure 21. Empirical relationship between seismic moment and rupture area for inland crustal earthquakes. The broken lines indicate the three-stage scaling relationships (after Irikura and Miyake, 2010).

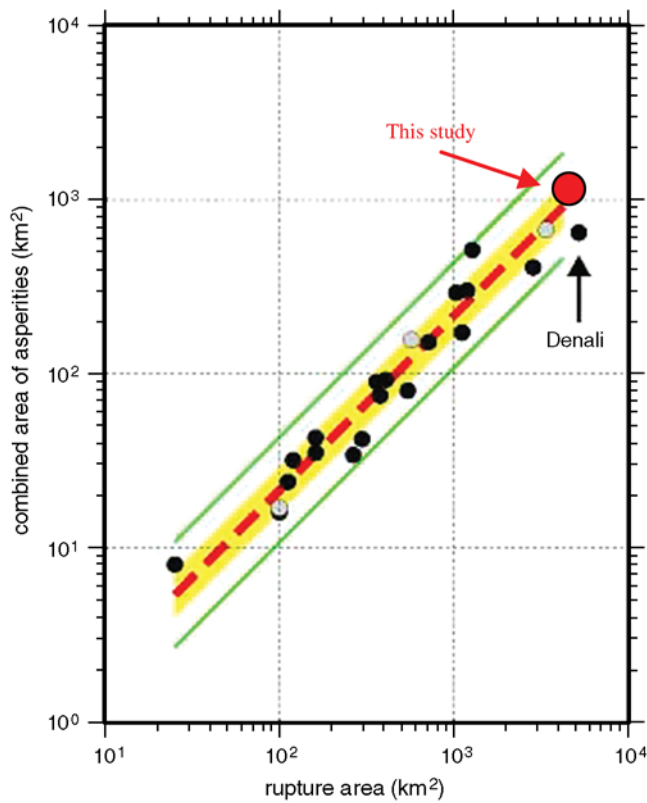


Figure 22. Empirical relationship between the combined area of asperities and the total rupture area for an inland crustal earthquake (after Irikura and Miyake, 2010). The open circle indicates the result of the present study. The shaded areas represent $\pm\sigma$ (standard deviation). The thin solid lines show factors of 2 and 1/2 of the average values. The database obtained by the waveform inversions is from Somerville *et al.* (1999) and Miyakoshi *et al.* (2000).

strong-motion seismograms used in this study were provided by the China Strong Motion Network Center of the Institute of Engineering Mechanics, belonging to the China Earthquake Administration. Data are available by applying to the China Strong Motion Network Center through their web site (www.csmnc.net/; last accessed June 2010).

The strong-motion records of the Natural Research Institute for Earth Science and Disaster Prevention (NIED) used in this article can be retrieved from the K-NET and KiK-net (www.kyoshin.bosai.go.jp/kyoshin/; last accessed June 2010). The moment tensor solution can be obtained from the F-net web site (www.fnet.bosai.go.jp/top.php; last accessed June 2010). The collapse ratios of buildings by the Chengdu Branch of the China Academy of Science are available on its web site (http://www.kepu.net.cn/gb/special/2009/0512/03_kj/03_1sl_02sl1.html; last accessed June 2010). We used Generic Mapping Tools (available at <http://gmt.soest.hawaii.edu/>; Wessel and Smith, 1995) to draw the figures.

Acknowledgments

We are deeply appreciative of comments provided by the associate editors and reviewers. We would like to express our gratitude to the China Strong Motion Network Center of Institute of Engineering and the National

Research Institute for Earth Science and Disaster Prevention, Japan, for providing important strong-motion data for the present study. This study was supported in part by Grants-in-Aid for Scientific Research (A) (grant number: 19201034) from the Ministry of Education, Culture, Sports, Science and Technology (MEXT, Monbu-Kagaku-Sho) of Japan.

References

- Akaike, H. (1973). Information theory and an extension of the maximum likelihood principle, in *2nd International Symposium on Information Theory*, B. N. Petrov and F. Csaki, (Editors), Akademia Kiado, Budapest, 267–281.
- Asano, K., T. Iwata, and K. Irikura (2005). Estimation of source rupture process and strong ground motion simulation of the 2002 Denali, Alaska, earthquake, *Bull. Seismol. Soc. Am.* **95**, 1701–1715.
- Bouchon, M. (1981). A simple method to calculate Green's functions for elastic layered media, *Bull. Seismol. Soc. Am.* **71**, 959–971.
- Brune, J. N. (1970). Tectonic stress and spectra of seismic shear waves from earthquakes, *J. Geophys. Res.* **75**, 4997–5009.
- Brune, J. N. (1971). Correction to Brune (1970), *J. Geophys. Res.* **76**, 5002.
- Chendu Branch of the China Academy of Science (2008). Rescue using science and technology for the 2008 Wenchuan earthquake, http://www.kepu.net.cn/gb/special/2009/0512/03_kj/03_1sl_02sl1.html (last accessed September 2010).
- China Earthquake Administration (2008). General introduction to engineering damage during Wenchuan M_S 8.0 earthquake, *J. Earthq. Eng. Eng. Vib.* **28**, Supplement, 1–114, <http://cegrg.cga.harvard.edu/content/engineering-damage-wenchuan-earthquake-october-2008> (last accessed September 2010).
- Geographical Survey Institute (2008). 2008 Chishuan earthquake, <http://cais-gsi.go.jp/YOCHIREN/activity/178/image178/022.pdf> (last accessed September 2010).
- Hanks, T. C., and W. H. Bakun (2002). A bilinear source-scaling model for $M - \log A$ observations of continental earthquakes, *Bull. Seismol. Soc. Am.* **92**, 1841–1846.
- Hisada, Y. (2006). Relation between asperity of seismic source and near-fault strong ground motion, in *Proc. of the 12th Japan Earthquake Engineering Symp.*, Tokyo, Japan, 3–5 November 2006, 186–189.
- Ikeda, Y., H. He, K. Kano, W. Lin, T. Ishiyama, H. Zhang, Z. Wei, and F. Shi (2008). *Geological reconnaissance of the source area for the Wenchuan, Sichuan Province, earthquake of May 12, 2008, Wenchuan earthquake, China*, Grant-in-Aid for Special Purposes of 2008, Ministry of Education, Culture, Sports, Science and Technology (MEXT), No. 20900002, 241–272.
- Irikura, K. (1986). Prediction of strong acceleration motions using empirical Green's function, *Proc. of the 7th Japan Earthquake Engineering Symp.*, Tokyo, Japan, 151–156.
- Irikura, K. (2004). Recipe for predicting strong ground motion from future large earthquake, *Disaster Prevention Institute Annals (Kyoto Daigaku Bosai Kenkyujo Nenpo)*, **47A**, 25–45 (in Japanese with English abstract).
- Irikura, K., and K. Kamae (1999). Strong ground motions during the 1948 Fukui earthquake—Estimation of broad-band ground motion using a hybrid simulation technique, *Zisin* **52**, 129–150 (in Japanese with English abstract).
- Irikura, K., and H. Miyake (2001). Prediction of strong ground motions for scenario earthquakes, *J. Geogr.* **110**, 849–875 (in Japanese with English abstract).
- Irikura, K., and H. Miyake (2010). Recipe for predicting strong ground motion from crustal earthquake scenarios, *Pure Appl. Geophys.*, <http://www.springerlink.com/content/424323g755p14436/>.
- Irikura, K., H. Miyake, T. Iwata, K. Kamae, and H. Kawabe (2002). Revised recipe for predicting strong ground motion and its validation, *Proc. of the 11th Japan Earthquake Engineering Symp.*, Tokyo, Japan, 20–22 November, 567–572 (in Japanese with English abstract).
- Iwata, T., and K. Irikura (1988). Source parameters of the 1983 Japan-Sea earthquake sequence, *J. Phys. Earth* **36**, 155–184.

- Ji, C., and G. Hayes (2008). Preliminary Result of the May 12, 2008 M_w 7.9 Eastern Sichuan, China Earthquake, http://earthquake.usgs.gov/earthquakes/eqinthenews/2008/us2008ryan/finite_fault.php (last accessed September 2010).
- Kamae, K., and K. Irikura (1998). Rupture process of the 1995 Hyogo-ken Nanbu earthquake and simulation of near-source ground motion, *Bull. Seismol. Soc. Am.* **88**, 400–412.
- Kamae, K., K. Irikura, and A. Pitarka (1998). A technique for simulating strong ground motion using hybrid Green's function, *Bull. Seismol. Soc. Am.* **88**, 357–367.
- Kitagawa, K. (1993). *Programming for Time Series Analysis*, Iwanami Shoten Inc., Tokyo, Japan, 390 pp. (in Japanese).
- Koketsu, K., Y. Yokota, H. Ghasemi, K. Hikima, H. Miyake, and Z. Wang (2009). *Source Process and Ground Motions of the 2008 Wenchuan Earthquake, Investigation report of the May 12th 2008, Wenchuan earthquake, China*, Grant-in-Aid for Special Purposes of 2008, Ministry of Education, Culture, Sports, Science and Technology (MEXT), No. 20900002, 201–212.
- Li, X. J., Z. Zhou, H. Yu, R. Wen, D. Lu, M. Huang, Y. Zhou, and J. Cui (2008). Strong motion observation and recordings from the great Wenchuan earthquake, *Earthq. Eng. Eng. Vib.* **7**, no. 3, 235–246.
- Liu, Q. Y., Y. Li, J. H. Chen, B. Guo, S. C. Li, J. Wang, X. Q. Zhang, and S. H. Qi (2009). Wenchuan M_s 8.0 earthquake: Preliminary study of the S-wave velocity structure of the crust and upper mantle, *Chin. J. Geophys.* **52**, no. 2, 309–319.
- Lou, H., C. Y. Wang, Z. Y. Lu, Z. X. Yao, S. G. Dai, and H. C. You (2008). Deep tectonic setting of the 2008 Wenchuan M_s 8.0 earthquake in southwestern China—Joint analysis of teleseismic P-wave receiver functions and Bouguer gravity anomalies, *Sci. China D Earth Ser.* **52**, 166–179.
- Madariaga, R. (1979). On the relation between seismic moment and stress drop in the presence of stress and strength heterogeneity, *J. Geophys. Res.* **84**, 2243–2250.
- Miyake, H., T. Iwata, and K. Irikura (1999). Strong ground motion simulation and source modeling of the Kagoshima-ken Hokuseibu earthquake of March 26 (Mjma 6.5) and May 13 (Mjma6.3), 1997, using empirical Green's function method, *Zisin* **51**, 431–442, (in Japanese with English abstract).
- Miyake, H., T. Iwata, and K. Irikura (2003). Source characterization for broadband ground-motion simulation: Kinematic heterogeneous source model and strong motion generation area, *Bull. Seismol. Soc. Am.* **93**, 2531–2545.
- Miyakoshi, K., T. Kagawa, H. Sekiguchi, T. Iwata, and K. Irikura (2000). Source characterization of inland earthquakes in Japan using source inversion results, *Proc. of the 12th World Conf. of Earthquake Engineering*, 1850, 8 pp.
- Shen, Z., Y. Wan, J. Sun, M. Wang, P. Zhang, W. Gan, Y. Zeng, and Q. Wang (2008). Coseismic rupture distribution of the 2008 Wenchuan China earthquake inferred using GPS and InSAR measurements, *American Geophysical Union*, Fall Meeting 2008, U22B-03.
- Somerville, P., K. Irikura, R. Graves, S. Sawada, D. Wald, N. Abrahamson, Y. Iwasaki, T. Kagawa, N. Smith, and A. Kowada (1999). Characterizing crustal earthquake slip models for the prediction of strong ground motion, *Seismol. Res. Lett.* **70**, 59–80.
- Suzuki, W., S. Aoi, and H. Sekiguchi (2008). Source process of the 2008 Iwate Miyagi nairiku earthquake derived from near-fault strong motion data, http://www.k-net.bosai.go.jp/k-net/topics/Iwatemiyaginairiku_080614/inversion/index.html last accessed September 2010 (in Japanese).
- Tsurugi, M., M. Tai, K. Irikura, and A. Kowada (1997). Estimation of empirical site amplification effects using observed record, *Zisin* **50**, 215–227 (in Japanese with English abstract).
- Wang, W. M., L. F. Zhao, J. Ki, and Z. X. Yao (2008). Rupture process of the M_s 8.0 Wenchuan earthquake of Sichuan, China, *Chin. J. Geophys.* **51**, no. 5, 1403–1410 (in Chinese).
- Watanabe, M., H. Fujiwara, T. Sato, T. Ishii, and T. Hayakawa (2008). Effects of complexity of fault rupture process on strong ground motions and extraction of the dominant parameters—Study on the rupture process of the 2003 Tokashi-Oki earthquake, *Zisin* **60**, 253–265 (in Japanese with English abstract).
- Wei, Z., Y. Shen, and X. F. Chen (2008). Numerical simulation of strong ground motion for the M_s 8.0 Wenchuan earthquake of 12 May 2008, *Sci. China D Earth Ser.* **51**, 1637–1682.
- Wessel, P., and W. H. F. Smith (1995). New version of the generic mapping tools released, *Eos Trans. AGU* **76**, 329.
- Yarai, H., T. Nishimura, M. Tobita, A. Suzuki, H. Suito, T. Imakiire, and H. Masahiro (2008). A fault model of the Wenchuan earthquake estimated from SAR measurements, *7th General Assembly of the Asian Seismological Commission*, Tsukuba, Japan, 24–27 November 2008.

Graduate School of Engineering
 Aichi Institute of Technology
 1247 Yachigusa, Yakusa-cho
 Toyota-shi, Aichi 470-0392, Japan
 susumu@aitech.ac.jp
 (S.K.)

Disaster Prevention Research Center
 Aichi Institute of Technology
 1247 Yachigusa, Yakusa-cho
 Toyota-shi, Aichi 470-0392, Japan
 irikura@geor.or.jp
 (K.I.)

Manuscript received 19 September 2009